sustainability

MDPI

Article

Global Food Security in a Climate-Oscillating World: Spectral Evidence and Early Warning Implications for Sustainable Food Systems

Kostiantyn Pavlov [1,2,*], Olena Pavlova [1,3], Oksana Liashenko [1,4,*], Tomasz Wołowiec [2], Maksym Zhytar [5], Sylwester Bogacki [2], Eleonora Tankova [6], Polina Puzyrova [7] and Olena Mykhailovska [5]

1 Department of Economics and Trade, Lesya Ukrainka Volyn National University, Voli Avenue 13, 43025 Lutsk, Ukraine; strishenez@gmail.com
2 Faculty of Administration and Social Sciences, WSEI University in Lublin, Projektowa 4, 20-209 Lublin, Poland; tomasz.wolowiec@wsei.pl (T.W.); sylwester.bogacki@wsei.pl (S.B.)
3 Faculty of Management, AGH University of Kraków, Gramatyka 10, 30-059 Krakow, Poland
4 Loughborough Business School, Loughborough University, Epinal Way, Loughborough LE11 3TU, UK
5 Faculty of Management, Finance and Marketing, National University «Kyiv Aviation Institute», Liubomyra Huzara Avenue 1, 03058 Kyiv, Ukraine; maksym.zhytar@kai.edu.ua (M.Z.); m-olena@ukr.net (O.M.)
6 Department of Administration and Management, Varna Free University, Yanko Slavchev 84, Chayka Resort, 9007 Varna, Bulgaria; eleonora.tankova@vfu.bg
7 Department of Economics, Kyiv National University of Technologies and Design, Mala Shyianovska Str. 2, 01011 Kyiv, Ukraine; puzyrova@ukr.net
* Correspondence: pavlovkostya@gmail.com (K.P.); o.liashenko@lboro.ac.uk (O.L.); Tel.: +380-972830808 (K.P.)

Abstract

In March 2022, the FAO Food Price Index peaked at 159.7 as climate shocks collided with geopolitical disruption, pushing global hunger past 735 million and exposing how deeply climate variability penetrates the economics of agri-food systems. Yet the imprint of ocean–atmosphere oscillations on global food prices—the central economic signal of the agri-food system—has not, to our knowledge, been mapped systematically in the frequency domain. This study delivers, to our knowledge, one of the first multi-oscillation cross-spectral analyses of the climate–food price nexus, matching 7 climate indices across the Pacific, Atlantic, and Indian Ocean basins with 5 disaggregated FAO Food Price Index sub-components over 432 monthly observations (1990–2025), verified through 6 robustness checks, including surrogate data testing. Four findings carry direct policy relevance. ENSO indicators lead global food prices by three to four months with a 100% surrogate test pass rate—one of the cleanest actionable climate–price signals documented to date. The Indian Ocean Dipole leads prices by roughly one to two years (cross-correlation peak at sixteen months, though the peak is broad and not sharply localised within that window), extending the early warning horizon well beyond the ENSO signal. The apparent Atlantic Multidecadal Oscillation–price correlation ($r \approx +0.60$) is revealed to be a common-trend artefact. Vegetable oils are the most consistently climate-exposed commodity chain across the seven oscillations; sugar and meat, often assumed less climate-sensitive, in fact show strong coherence with specific oscillations (sugar with the Indian Ocean Dipole and meat with the Southern Oscillation Index), indicating that commodity-level exposure is oscillation-specific rather than uniform and reflects each commodity's position in the production-to-consumption chain—short-cycle, thinly buffered commodities transmit weather shocks to price quickly, while feed-market intermediation delays and smooths the pass-through for livestock. These results provide the empirical foundation for integrating real-time monitoring of climate oscillations into food system governance—a low-cost policy innovation that aligns economic stability objectives with climate adaptation goals, strengthens the resilience of agri-food value chains, and supports progress towards Sustainable Development Goal 2 (Zero Hunger).

Check for updates

Academic Editors: Konstadinos Abeliotis and Ilija Djekic

Received: 22 July 2026
Revised: 7 September 2026
Accepted: 11 September 2026
Published: 15 September 2026

Copyright: © 2026 by the authors. Licensee MDPI, Basel, Switzerland. This article is an open access article distributed under the terms and conditions of the Creative Commons Attribution (CC BY) license.

Keywords: global food security; sustainable food systems; SDG 2; climate oscillations; ENSO; Indian Ocean Dipole; FAO Food Price Index; early warning systems; agri-food value chains; food price volatility

1. Introduction

Feeding the world sustainably is one of the defining challenges of the twenty-first century. In 2023, an estimated 735 million people were chronically undernourished, and more than 2.3 billion faced moderate or severe food insecurity [1]. The FAO Food Price Index (FPI) peaked at 159.7 in March 2022, driven by the Russia–Ukraine conflict, post-pandemic supply chain disruptions, and adverse weather across major breadbaskets [2]. These recurring price shocks threaten progress towards Sustainable Development Goal 2 (Zero Hunger) and expose deep structural vulnerabilities in the global food system [3].

A growing body of evidence suggests that large-scale ocean–atmosphere oscillations are a persistent, yet insufficiently understood, source of global food price variability. The El Niño–Southern Oscillation (ENSO), the dominant mode of interannual climate variability with a characteristic periodicity of 2–7 years [4], affects crop yields on more than a quarter of the world's cultivated land [5]. El Niño events reduce maize yields by up to 4.3% globally while boosting soybean yields by 2–5%, and La Niña years are associated with below-normal yields across all major staple crops. Iizumi et al. [5] report these directional yield responses as statistically significant at conventional levels, although effect magnitudes vary by region and crop. Ray et al. [6] estimated that climate variability explains 32–39% of year-to-year yield variability worldwide, with substantially higher fractions in key breadbasket regions. Beyond ENSO, other oscillations—the Indian Ocean Dipole (IOD), the Pacific Decadal Oscillation (PDO), the Atlantic Multidecadal Oscillation (AMO), and the North Atlantic Oscillation (NAO)—modulate regional temperature and precipitation patterns on timescales ranging from biennial to multidecadal [7–9], yet their effects on global food prices have received comparatively little attention.

Yield responses are not uniform across production systems. Agro-Ecological Zones (AEZs) differ systematically in their exposure: rainfed systems in semi-arid and sub-humid tropical zones—much of sub-Saharan Africa, South Asia, and northeastern Brazil—translate ENSO-driven precipitation anomalies almost directly into yield shocks, whereas irrigated systems in temperate zones (the U.S. Midwest, the North China Plain, parts of Europe) buffer short-run rainfall deficits through stored or diverted water, so the same climate oscillation signal produces a materially smaller production response. Tropical production zones are also more exposed to IOD- and ENSO-linked monsoon disruption, while temperate zones are more sensitive to NAO- and AMO-related temperature and storm-track shifts. This AEZ-level heterogeneity is a plausible physical mechanism underlying the commodity-specific coherence patterns we later document at the price level (Section 5.5): commodities sourced disproportionately from rainfed tropical AEZs (e.g., cereals from South Asian and Sahelian smallholder systems, and cocoa and palm oil from tropical rainfed plantations) would be expected to show tighter climate–price coupling than commodities sourced from irrigated temperate systems, providing an agronomic foundation for the sub-index differentiation tested under H4.

Existing empirical research on the climate–food price nexus has operated almost exclusively in the time domain. Cashin et al. [10] used a global vector autoregressive (VAR) model to show that El Niño shocks raise non-fuel commodity prices, with effects peaking at lags of 4–8 months. Ubilava [11] demonstrated that ENSO effects on wheat prices are nonlinear and asymmetric across El Niño and La Niña phases. Headey and Fan [12]

identified a confluence of weather, biofuel, and trade policy drivers behind the 2007–2008 food price crisis. These time-domain approaches provide valuable estimates of average effects, but they are less naturally suited to decomposing the climate–price relationship by frequency: they do not reveal which cyclical components of climate variability are transmitted to food prices, nor at what timescales the transmission is strongest.

The frequency domain provides a natural framework for addressing these questions. Cross-spectral coherence—the frequency-domain analogue of the correlation coefficient—measures the strength of the linear association between two time series at each frequency, while the phase spectrum identifies lead–lag relationships at each frequency [13]. These tools have a long history in climatology, where they have been used to characterise ENSO dynamics [4] and to study the modulation of climate signals across ocean basins [14]. In economics, spectral methods have been applied to business cycle synchronisation [15] and commodity price co-movement [16], but their application to the climate–food price nexus remains limited.

The closest antecedent to the present study is Cai and Sakemoto [17], who used partial wavelet coherence to examine the relationship between the Southern Oscillation Index (SOI) and aggregate commodity price indices. They found significant coherence at 32–64 and 64–128 months, with the relationship strengthening after 2000. However, their analysis was restricted to a single climate index (SOI) and to aggregate commodity categories that included metals, energy, and food. We would add that the FAO FPI is not a pure agricultural fundamentals index: its dairy and vegetable oil sub-components, in particular, embed processing and energy costs, so part of the divergence between our results and those of Cai and Sakemoto reflects differences in the energy intensity of the two price measures rather than differences in climate transmission alone. The questions of how multiple, simultaneously operating climate oscillations interact with food prices, and whether different food commodities respond to distinct climate signals, remain unanswered.

More recently, Pavlova et al. [18] applied wavelet coherence to the FAO FPI and the Prevalence of Undernourishment (SDG 2.1.1) over 2001–2023, finding that although raw coherence was strong ($R^2 \approx 0.77$), only 7.8% of time–frequency cells were statistically significant against an AR(1) null, with significant co-movement clustering at medium-run horizons of 3–6 years. This finding underscores the need for rigorous significance testing and motivates the present study's use of IAAFT surrogate testing. The apparently low share of significant cells in Pavlova et al.'s work reflects the stringency of pointwise time–frequency testing against an AR(1) null across the full scalogram. The present study improves on that design by combining a bivariate cross-spectral estimator with IAAFT surrogates, which target the specific null of no inter-series coupling and thereby isolate the frequency bands at which climate signals are genuinely transmitted to prices.

This paper addresses these gaps at two distinct levels. The methodological novelty is comparative rather than absolute: individual components of our toolkit—Welch coherence, wavelet coherence, and IAAFT surrogate testing—are well established in climatology and, increasingly, in commodity price research (Section 2.4). What is new here is their joint application, with a shared significance framework and cross-validation between estimators, to seven climate oscillation indices simultaneously against five disaggregated FAO Food Price Index sub-components. To our knowledge, no prior study has applied this combination at this scope. We phrase this as "to our knowledge, one of the first" rather than "the first" in the Abstract, since we cannot exhaustively rule out unpublished or non-English-language precedents. The empirical novelty is the specific pattern of results this scope reveals (Section 5): a robust 3–4-month ENSO lead, a food price coherence structure for the six non-ENSO oscillations that is considerably more fragile under scrutiny than the

raw correlations suggest (Sections 5.7 and 6.1), and commodity-specific rather than uniform sub-index sensitivity (Section 5.5). We match seven climate oscillation indices—Niño 3.4, SOI, the Multivariate ENSO Index (MEI v2), IOD, NAO, PDO, and AMO—with the five sub-components of the FAO Food Price Index (cereals, meat, dairy, vegetable oils, and sugar) over the period January 1990 to December 2025 (432 monthly observations). The methodological framework combines Welch power spectral density estimation [19], magnitude-squared cross-spectral coherence with phase analysis [13], continuous wavelet coherence [20,21], lagged cross-correlation, and rolling-window coherence. The robustness of the findings is assessed through six sensitivity checks, including first-differencing, alternative spectral estimators (Thomson's multitaper method [22]), sub-period stability analysis, and Iterative Amplitude-Adjusted Fourier Transform (IAAFT) surrogate testing [23].

The study contributes to the sustainability literature in five respects. First, it reveals that ENSO indicators robustly lead global food prices by 3 to 4 months in the 2–3-year frequency band, with a 100% pass rate in surrogate data testing—the cleanest and most policy-actionable finding. Second, it shows that the Indian Ocean Dipole provides a 16-month lead on food prices, potentially extending the early warning horizon beyond the reach of conventional weather-based approaches. Third, it demonstrates that the strong time-domain correlation between the AMO and food prices ($r = +0.60$) is largely an artefact of common trends, underscoring the need for frequency-domain methods to distinguish genuine oscillatory couplings from spurious co-movement. Fourth, it disaggregates the analysis by food commodity, revealing that dairy and vegetable oils are the most climate-sensitive categories, while meat is buffered by feed-market intermediation. Fifth, it tests whether the climate–food price nexus has strengthened since 2008 and finds no statistically defensible evidence that it has: the apparent post-2008 increase in PDO–FPI and NAO–FPI coherence under a parametric Fisher z-test does not survive a block-bootstrap correction for the small effective number of spectral estimates per sub-period, while ENSO coherence remains structurally stable across sub-periods.

These findings have direct implications for the design of climate-informed early warning systems under SDG 2, the prioritisation of adaptation investments in sustainable food systems, and the integration of real-time monitoring of climate oscillations into food security governance. More broadly, the paper demonstrates that global food prices contain embedded climate signals that can be identified, attributed to specific ocean basins and timescales, and potentially exploited to protect the world's most food-insecure populations.

2. Literature Review

This section synthesises four streams of literature that converge on the relationship between climate variability and food price dynamics: (i) the agroclimatic evidence linking large-scale climate oscillations to crop yields, (ii) the transmission of climate shocks to global commodity prices, (iii) the economics of extreme weather events and natural disasters, and (iv) the methodological evolution of spectral and wavelet techniques in climate–economy research. Each stream is reviewed in turn, after which the research gap at its intersection is identified.

2.1. Climate Oscillations and Crop Yield Variability

The El Niño–Southern Oscillation (ENSO) is the dominant mode of interannual climate variability, with a characteristic periodicity of 2–7 years [4]. Its influence on regional precipitation, temperature, and cloud cover has been extensively documented [24]. The agronomic consequences of ENSO are now well established at the global scale. Iizumi et al. [5], analysing gridded yield data for maize, rice, wheat, and soybean, demonstrated that El

Niño events improve global-mean soybean yields by 2.1–5.4% but reduce maize yields by up to 4.3%, while La Niña years are associated with below-normal yields across all four crops. Their findings imply that ENSO affects more than a quarter of the world's croplands, making it a systematic rather than idiosyncratic risk factor.

Ray et al. [6] extended this line of inquiry by showing that climate variability explains approximately 32–39% of year-to-year yield variability globally, with substantially higher fractions (exceeding 60%) in key breadbasket regions. Importantly, the magnitude and even the sign of the ENSO effect are spatially heterogeneous: El Niño tends to reduce yields in Australia, southern Africa, and parts of South and Southeast Asia, while benefiting regions in South America [25]. This spatial heterogeneity, combined with the structure of global agricultural trade, creates a potential for geographically correlated production shocks to be transmitted to international commodity prices [26].

Beyond ENSO, other large-scale climate oscillations have received comparatively less attention in the agricultural literature. The Indian Ocean Dipole (IOD) modulates monsoon rainfall over South and Southeast Asia, affecting rice and wheat production in India and Indonesia [7]. The Atlantic Multidecadal Oscillation (AMO) operates on multidecadal timescales and has been linked to shifts in the Sahel rainfall regime and European summer temperatures [27]. The Pacific Decadal Oscillation (PDO) modulates the background state against which ENSO events unfold, potentially amplifying or dampening their agricultural impacts [28]. However, quantitative assessments of the effects of these non-ENSO oscillations' effects on global food production remain sparse.

2.2. Climate Shocks and Global Food Commodity Prices

The transmission of climate-induced production shortfalls to international food prices operates through a multi-stage supply chain encompassing farm-gate production, storage, trade, and processing [12]. The global food price crises of 2007–2008 and 2010–2011 catalysed substantial research into the drivers of price volatility. Headey and Fan [12] identified a confluence of factors—including weather shocks, biofuel mandates, export restrictions, and speculative trading—that contributed to the 2007–2008 crisis, with no single cause predominating.

Ubilava [11] directly examined the ENSO–commodity price nexus using a regime-switching framework and found that ENSO exerts significant, but nonlinear, effects on the global prices of wheat, maize, rice, and soybeans. His results demonstrated that the impact is asymmetric across ENSO phases and varies by commodity, with rice and soybean prices being particularly sensitive to El Niño events. Cashin et al. [10] confirmed these findings using a global VAR model, reporting that a positive El Niño shock raises non-fuel commodity prices, with the effect peaking at a lag of approximately 4–8 months.

Most recently, Cai and Sakemoto [17] employed partial wavelet coherence (PWC) to investigate the ENSO–commodity price relationship in the time–frequency domain. They found significant coherence between the Southern Oscillation Index (SOI) and agricultural, food, and raw material commodity prices at lower frequencies (32–64 and 64–128 months), with this relationship strengthening markedly after 2000. Pavlova et al. [18] extended the frequency-domain approach to food security, showing that only 7.8% of FPI–PoU wavelet coherence cells achieved significance and documenting a regime change around 2012. These studies represent the closest antecedents but are limited to single climate indices and aggregate categories.

A parallel strand of literature has applied wavelet coherence to examine the drivers of food commodity price co-movement. Frimpong et al. [29] demonstrated that global economic policy uncertainty drives agricultural commodity market connectedness across multiple time–frequency scales. More recently, wavelet coherence has been used to link

FAO Food Price Index (FPI) sub-components to geopolitical risk and climate policy uncertainty indices, revealing heterogeneous co-movement patterns across frequency bands (2025). However, none of these studies incorporated physical climate oscillation indices as explanatory variables.

2.3. The Economics of Extreme Weather Events

The economic analysis of weather-related disasters has evolved considerably since the seminal contribution of Nordhaus [30], who demonstrated that U.S. hurricane damage scales approximately with the ninth power of maximum wind speed. Strobl [31] refined this analysis at the county level, finding that hurricane strikes reduce annual economic growth by 0.45 percentage points in affected U.S. coastal counties, with approximately 28% of this effect attributable to out-migration of wealthier residents. Botzen et al. [32] provided a comprehensive review of the economic costs of natural disasters, emphasising the distinction between direct asset destruction and indirect losses arising from supply chain disruption, trade interruptions, and price transmission.

The food system dimension of extreme weather economics has gained prominence following the compounding effects of the COVID-19 pandemic and the Ukraine conflict on global food markets. Extreme weather events such as tropical cyclones can severely disrupt agricultural supply chains, destroying crops ready for harvest and disabling port infrastructure critical to food trade [30–32]. The 2022 food price crisis, during which the FAO Food Price Index reached its historical maximum of 159.7, illustrated how supply-side shocks interact with geopolitical disruptions to produce unprecedented price spikes [1].

However, the disaster economics literature has predominantly operated in the time domain, analysing the magnitude and duration of price shocks following specific events. The frequency-domain structure of the climate–food price relationship—that is, which cyclical components of climate variability transmit to food prices, and at what timescales—remains largely unexplored.

2.4. Spectral and Wavelet Methods in Climate–Economy Research

The methodological foundations for the present study draw on the spectral analysis tradition in both climatology and economics. Torrence and Compo [4] established the canonical framework for wavelet analysis of climate time series, developed significance tests against red-noise backgrounds, and demonstrated their application to the ENSO system. Their work revealed significant multidecadal modulation of ENSO variance, with higher power during 1880–1920 and 1960–1990 and lower power during 1920–1960.

In the frequency domain, cross-spectral analysis—comprising coherence (the frequency-domain analogue of correlation) and phase analysis (revealing lead–lag relationships)—provides a natural framework for investigating whether two time series share cyclical components and, if so, which series leads. Granger and Watson [33] provided the foundational treatment of spectral methods in econometrics, noting that while spectral analysis is informationally equivalent to time-domain methods, it offers unique advantages for detecting cyclical co-movement that may be masked in standard regression or VAR frameworks.

The wavelet coherence approach extends classical cross-spectral analysis by allowing the coherence to vary over time, thus accommodating the non-stationarity inherent in both climate and economic systems. Vacha and Barunik [16] demonstrated the utility of this approach for commodity price analysis, revealing that co-movement between energy commodities is frequency dependent and time-varying. Aguiar-Conraria et al. [15] applied continuous wavelet transforms to study business cycle synchronisation, establishing methodological precedents for the time–frequency analysis of economic phenomena.

2.5. Identification of the Research Gap

The review above reveals that three well-developed literatures—ENSO and crop yields, climate shocks and commodity prices, and spectral/wavelet methods—have evolved largely in isolation from one another. Their intersection defines a clear and substantive research gap.

First, the agroclimatic literature (Section 2.1) has established that ENSO, and to a lesser extent IOD and AMO, affect crop yields globally. However, this literature operates predominantly in the time domain and at the level of physical production, without extending the analysis to the price transmission mechanism. The dependent variable is typically yield (tonnes per hectare), not price.

Second, the commodity price literature (Section 2.2) has begun to examine the ENSO–price nexus using time–frequency methods, but with important limitations. Cai and Sakemoto [17]—the most closely related study—used only a single climate index (SOI) and aggregate commodity price categories, without disaggregating the FAO Food Price Index into its five sub-components (cereals, meat, dairy, vegetable oils, and sugar). Other climate oscillations (AMO, PDO, IOD, NAO, and MEI) that operate on different timescales and affect different agricultural regions have not been examined in the frequency domain.

Third, the frequency-domain link between climate oscillations and food price cycles has not been systematically mapped across multiple oscillations and commodity sub-indices. The companion question of how this price signal ultimately propagates to food security outcomes, such as the Prevalence of Undernourishment (PoU; SDG indicator 2.1.1), is addressed separately, using annual data over a longer horizon, in related work [18], and is outside the scope of the present monthly frequency analysis.

Fourth, the disaster economics literature (Section 2.3) provides rich evidence on localised, event-specific impacts but lacks a systematic frequency-domain perspective on how the cyclical structure of climate variability is embedded in global food prices. The question of whether food price cycles are phase-locked to specific climate oscillations—and if so, with what lead time—has not been addressed.

2.6. Hypotheses

Drawing on the four streams of literature reviewed above—climate–yield relationships, climate–price transmission, the economics of weather shocks, and spectral methods—we formulate five testable hypotheses. Each is grounded in the mechanisms established in Sections 2.1–2.4 and is evaluated against the spectral evidence in Section 5:

H1. *(ENSO–Price Coherence). The FAO Food Price Index and its sub-indices exhibit statistically significant cross-spectral coherence with ENSO-related climate indices (Niño 3.4, SOI, and MEI) in the 2–7-year frequency band, consistent with the known periodicity of the ENSO cycle and its documented influence on global crop yields [5,17].*

H2. *(Multi-Oscillation Heterogeneity). Climate oscillations operating on different timescales—ENSO (2–7 years), IOD (biennial), and the PDO and AMO (decadal to multidecadal)—are each associated with food price variability at their respective characteristic frequencies, implying that global food prices contain multiple embedded climate signals rather than a single dominant cycle.*

H3. *(ENSO, IOD, and PDO Lead Prices). Phase and lagged cross-correlation analysis reveal that the ENSO, IOD, and PDO indices lead FAO FPI sub-indices by 2–16 months (while the AMO is not expected to lead prices, its association being hypothesised to operate through shared low-frequency trends), reflecting the biological and logistical lags in the climate → production → market → price transmission chain documented for ENSO shocks [10].*

H4. *(Sub-Index Differentiation). The five FAO FPI sub-indices (cereals, meat, dairy, vegetable oils, and sugar) exhibit heterogeneous coherence profiles across different climate oscillations, reflecting commodity-specific exposure to climate variability through production geography and supply chain structure—with commodities further removed from direct weather impacts through feed-market intermediation (meat and dairy) hypothesised to show weaker, more lagged coherence.*

H5. *(Strengthening Climate–Price Nexus). The coherence between climate oscillation indices and food prices has strengthened over time, particularly after 2000, consistent with the intensification of climate variability under anthropogenic warming and with prior evidence of strengthening ENSO–commodity coherence [17] and projected increases in extreme ENSO events [34].*

3. Data

3.1. FAO Food Price Index

The primary dependent variable is the FAO Food Price Index (FPI), a trade-weighted index of international food commodity prices published monthly by the Food and Agriculture Organisation of the United Nations [2]. The index comprises five sub-indices—cereals, meat, dairy, vegetable oils, and sugar—each constructed from a basket of representative commodity price quotations weighted by average export shares for the 2014–2016 base period. The monthly FPI is available from January 1990 to December 2025, yielding 432 observations. For long-run spectral analysis, we additionally employ the annual FPI series covering 1961–2025 (65 observations). The annual series is used solely to corroborate the presence of low-frequency (multi-year) spectral power in the price record that the 1990–2025 monthly window resolves only imprecisely—it is not analysed at the sub-index level, and all coherence, phase, and surrogate results reported in Section 5 are based on the monthly 1990–2025 sample. Over the sample period, the FPI ranges from a historical low of 50.5 (May 2002) to an all-time high of 159.7 (March 2022), with the latter coinciding with the onset of the Russia–Ukraine conflict and associated disruptions to Black Sea grain exports.

3.2. Climate Oscillation Indices

We assemble monthly time series for seven climate oscillation indices that capture the dominant modes of ocean–atmosphere variability across the Pacific, Atlantic, and Indian Ocean basins. All indices are obtained from the U.S. National Oceanic and Atmospheric Administration (NOAA).

Three indices capture different aspects of the El Niño–Southern Oscillation (ENSO). The Niño 3.4 SST anomaly measures sea surface temperature departures from the 1991–2020 climatology in the central equatorial Pacific (5° N–5° S, 170° W–120° W), computed from the Extended Reconstructed SST version 5 dataset (ERSSTv5 [35]). The Southern Oscillation Index (SOI) captures the atmospheric component of ENSO as the standardised sea-level pressure differential between Tahiti and Darwin [36]. The Multivariate ENSO Index version 2 (MEI v2) integrates five atmospheric and oceanic variables over the tropical Pacific into a single bimonthly index [37].

The remaining four indices represent non-ENSO modes of climate variability. The Indian Ocean Dipole Mode Index (IOD/DMI) is computed as the SST anomaly gradient between the western and eastern tropical Indian Ocean [7,38]. The North Atlantic Oscillation (NAO) index measures the normalised sea-level pressure difference between the Azores and Iceland [36,39]. The Pacific Decadal Oscillation (PDO) represents the leading principal component of North Pacific monthly SST variability poleward of 20° N [8,40]. The Atlantic Multidecadal Oscillation (AMO) is defined as the area-weighted average SST anomaly over the North Atlantic (0–60° N), computed from ERSSTv5 [9,40].

All climate indices are merged with the FAO FPI data on year–month keys. The IOD series contains eight missing values (1.9%) at the end of 2025, which are interpolated linearly. All other series are complete over the 1990–2025 estimation window.

3.3. Food Security and Country-Level Data

To link the frequency-domain analysis of food prices to food security outcomes, we employ the Prevalence of Undernourishment (PoU; SDG indicator 2.1.1), defined as the share of the population whose habitual food consumption is insufficient to provide the dietary energy levels required for maintaining a normal, active, and healthy life [1]. The global PoU series is available annually for 2001–2023 (23 observations), ranging from a minimum of 7.3% in 2018 to a maximum of 12.9% in 2002. We additionally compile a country-level panel dataset for 190 countries over the period 2000–2023, incorporating food import dependency (food imports as a percentage of total merchandise imports), GDP per capita (constant 2015 USD), and country-level PoU, all sourced from the World Bank's World Development Indicators [41].

3.4. Summary Statistics

Table 1 summarises the data sources, coverage, and frequency of all variables used in the analysis. Table 2 presents descriptive statistics for the monthly estimation sample (N = 432).

Table 1. Data sources and coverage.

Variable	Acronym	Period	N	Frequency	Source
FAO Food Price Index	FPI	1990–2025	432	Monthly	FAO [2]
Cereals sub-index	—	1990–2025	432	Monthly	FAO [2]
Meat sub-index	—	1990–2025	432	Monthly	FAO [2]
Dairy sub-index	—	1990–2025	432	Monthly	FAO [2]
Vegetable oils sub-index	—	1990–2025	432	Monthly	FAO [2]
Sugar sub-index	—	1990–2025	432	Monthly	FAO [2]
FAO FPI (annual)	FPI	1961–2025	65	Annual	FAO [2]
Niño 3.4 SST anomaly	Niño 3.4	1950–2026	914	Monthly	NOAA CPC [36] (ERSSTv5 [35])
Southern Oscillation Index	SOI	1951–2025	900	Monthly	NOAA CPC [36]
Multivariate ENSO Index	MEI v2	1979–2026	566	Monthly	NOAA PSL [38]
Indian Ocean Dipole	IOD/DMI	1870–2025	1864	Monthly	NOAA PSL [38] (HadSST)
North Atlantic Oscillation	NAO	1950–2026	914	Monthly	NOAA CPC [36]
Pacific Decadal Oscillation	PDO	1854–2026	2066	Monthly	NOAA NCEI [40] (ERSSTv5 [35])
Atlantic Multidecadal Osc.	AMO	1854–2026	2066	Monthly	NOAA NCEI [40] (ERSSTv5 [35])
Prevalence of Undernourish.	PoU	2001–2023	23	Annual	FAO [1]/World Bank [41]
Country panel (food imports, GDP p.c., PoU; 190 countries)	—	2000–2023	4362	Annual	World Bank WDI [41]

Table 2. Descriptive statistics, monthly sample (January 1990–December 2025, N = 432).

Variable	Mean	S.D.	Min.	Max.	Missing
FPI	88.9	27.3	50.5	159.7	—
Cereals	86.7	27.8	45.0	170.1	—
Meat	86.1	20.3	56.1	125.4	—
Dairy	97.1	39.7	41.4	232.0	—
Oils	83.4	37.7	35.3	180.3	—
Sugar	91.2	36.2	43.1	198.4	—
Niño 3.4 (°C anomaly)	−0.02	0.87	−1.76	2.72	0
SOI	0.13	0.95	−3.10	2.90	0
MEI v2	−0.14	0.95	−2.42	2.61	0
IOD/DMI	0.01	0.34	−1.11	1.28	8
NAO	0.04	1.05	−3.18	2.63	0
PDO	−0.64	1.24	−4.21	2.55	0
AMO (°C)	0.43	0.34	−0.38	1.44	0

Notes: FPI and sub-indices are rebased to 2014–2016 = 100. Niño 3.4 is expressed as an SST anomaly (°C) relative to the 1991–2020 climatology, consistent with the other climate indices. All climate indices are dimensionless anomalies except Niño 3.4 and AMO (°C). Missing values refer to the merged monthly sample.

4. Methodology

This section describes the spectral and time–frequency methods employed to investigate the relationship between climate oscillation indices and FAO Food Price Index (FPI) sub-components. The methodological framework proceeds in five stages: (i) pre-processing and stationarity testing, (ii) power spectral density estimation, (iii) cross-spectral coherence and phase analysis, (iv) lagged cross-correlation analysis, and (v) wavelet coherence analysis. All computations are implemented in Python 3.12 using the SciPy 1.18.1 [42], NumPy 2.4.6 [43], and PyCWT 0.5.0b0 libraries.

4.1. Pre-Processing and Stationarity

Spectral analysis requires covariance (weak) stationarity—that is, the mean is constant and the autocovariance structure depends only on the lag and not on time [13]. Given that both the FAO FPI and several climate indices exhibit secular trends over the 1990–2025 sample (notably the upward trend in FPI and AMO), all series are linearly detrended prior to spectral estimation. We rely on linear detrending together with the robustness provided by first-differencing (Section 5.7.1) and the multitaper estimator (Section 5.7.4) rather than on band-pass pre-filtering. Band-pass filters, such as the Hodrick–Prescott or Christiano–Fitzgerald filters, impose a chosen pass-band and can themselves induce spurious oscillatory artefacts at the band edges (the Slutsky–Yule effect)—because our aim is to let the data reveal the operative frequencies rather than to pre-select them, we prefer estimators that do not fix a band in advance. We acknowledge, however, that linear detrending can distort the multidecadal structure of the AMO and PDO, whose low-frequency estimates should, therefore, be read with the caution noted in the Limitations. The 1990–2025 estimation window is dictated by the availability of the disaggregated FAO FPI sub-indices, which begin in 1990. Although individual climate indices extend much further back (in some cases to the nineteenth century), the analysis is deliberately confined to the common overlap with the price data. We note that this 36-year window spans only one to two full cycles of the multidecadal AMO and PDO, so their low-frequency spectral

estimates are correspondingly less precise. The annual FPI series (1961–2025) is used to partially probe these longer scales, and the limitation is revisited in Section 8. Formally, for each series $\{x_t\}$, we compute $\widetilde{x}_t = x_t - (\hat{\alpha} + \hat{\beta}t)$, where $\hat{\alpha}$ and $\hat{\beta}$ are ordinary least squares estimates of the intercept and slope, respectively.

Stationarity is assessed using the Augmented Dickey–Fuller (ADF) test [44] with a trend term included directly in the test regression (the "ct" specification), applied to each raw (non-pre-detrended) series. Including the trend within the test regression is necessary because prior linear detrending alters the sampling distribution of the test statistic, so that applying the standard constant-only ADF regression to an already-detrended series yields critical values that are not valid for that series. As a stricter robustness check, the Phillips–Perron (PP) test [45] is also applied with the same trend specification. This test is non-parametric with respect to serial correlation in the error term and is more conservative than ADF in finite samples. For series for which the null of a unit root cannot be rejected at the 5% level by either test, first-differencing is applied, and spectral analysis is conducted on the differenced series, with results reported separately. Under this procedure (Appendix B, Table A2), the FPI, cereals, meat, and sugar sub-indices do not reject the unit-root null under either test, and dairy and oils reject it under ADF but not under the stricter PP test. All seven climate indices reject the unit-root null under both tests. Given that most of the price series are not clearly stationarised by linear detrending alone, the first-differenced specification (Section 5.7.1) is treated as a co-primary check on all headline coherence results involving the FPI or its sub-indices, rather than as a supplementary robustness test. Findings that do not survive first-differencing are flagged accordingly in the Results and Discussion, and this limitation is revisited in Section 8.

Because coherence between two series that each retain a strong annual cycle can arise from that shared seasonality rather than from any economic transmission, the seasonal structure of the price series was examined directly. Regressing each detrended FPI series on twelve monthly dummies removes between 0.08% and 1.03% of its variance (FPI 0.08%, dairy 0.09%, sugar 0.30%, cereals 0.34%, oils 0.37%, and meat 1.03%), indicating that the FAO indices carry no material annual cycle—as expected for internationally traded commodity aggregates sourced from both hemispheres, in which opposing harvest calendars largely offset one another. As a robustness check, all cross-spectral results were nonetheless re-estimated with both the price and climate series deseasonalised by monthly dummies in addition to linear detrending. The maximum coherence values are unchanged to three decimal places for Niño 3.4 (0.719), SOI (0.662), PDO (0.806), AMO (0.657), and MEI (0.618), and change only marginally for NAO (0.667 → 0.666) and the IOD (0.700 → 0.657). The periods at which the maxima occur, and the number of significant frequency bins, are likewise essentially unaffected. Seasonal contamination, therefore, does not account for the coherence structure reported in Section 5, and the detrended (non-deseasonalised) specification is retained throughout for comparability with the wider literature. Niño 3.4 is used in anomaly form (Section 3.2), which removes the annual cycle on the climate side by construction.

The Indian Ocean Dipole (IOD) series contains eight missing values (1.9% of the monthly sample) at the end of 2025. These are imputed using linear interpolation, which preserves the spectral properties of the series for the frequencies of interest (periods > 6 months). No other imputation for missing data is required. Because the eight missing values lie at the terminal boundary of the record and represent 1.9% of the sample, we prefer linear interpolation to spline or model-based imputation, which can introduce spurious curvature at the series end. As the affected span is short relative to the lowest resolved periods, the impact on multi-year spectral estimates is negligible. We verified that excluding 2025 entirely leaves the coherence peak unchanged in magnitude

and location. The lagged lead–lag estimate for the IOD is, however, more sensitive to the series end and should be read with corresponding caution.

4.2. Power Spectral Density Estimation

The power spectral density (PSD) of each detrended series is estimated using Welch's method [19], which partitions the time series into overlapping segments, applies a window function to each segment, computes the periodogram of each windowed segment, and averages the resulting periodograms to obtain a consistent spectral estimate. This approach reduces the spectral estimate's variance at the cost of a modest loss of frequency resolution, a trade-off appropriate for our sample of 432 monthly observations. The baseline segment length L = 128 months (≈10.7 years) and 50% overlap follow the standard recommendation of Welch [19]: a 50% Hann-tapered overlap is near-optimal for variance reduction with correlated segments, while L = 128 is the shortest power-of-two segment that still resolves the lower edge of the 2–7-year ENSO band given monthly sampling. The sensitivity of all results to this choice is examined in Section 4.8.2 (L = 96 and L = 160).

Specifically, we partition each series into segments of length L = 128 months (approximately 10.7 years) with an overlap of D = 64 months (50%), yielding $K = \lfloor (N - D)/(L - D) \rfloor = 5$ approximately independent segments. Each segment is tapered with a Hann window to reduce spectral leakage. The PSD is then estimated as the average of the K modified periodograms:

$$\hat{S}_{xx}(f) = (1/K) \sum^{k} |X^{k}(f)|^{2},$$

where $X^{k}(f)$ denotes the discrete Fourier transform of the k-th windowed segment. The resulting PSD estimates have a frequency resolution of $\Delta f = f_s/L = 12/128 \approx 0.094$ cycles per year, corresponding to a longest resolvable period of approximately 10.7 years. The Nyquist frequency is $f_n = f_s/2 = 6$ cycles per year (period = 2 months). Dominant spectral peaks are identified using the SciPy find_peaks algorithm applied to the log-transformed PSD, with a prominence threshold of 0.3 log-units.

4.3. Cross-Spectral Coherence and Phase Analysis

The cross-spectral density between each climate index c_t and each FPI sub-index y_t is estimated using the same Welch segmentation and windowing parameters as for the PSD. The cross-spectral density is defined as:

$$\hat{S}^{c}_{\gamma}(f) = (1/K) \sum^{k} C^{k} * (f) \cdot Y^{k}(f),$$

where $C^{k}(f)$ denotes the complex conjugate of the Fourier transform of the climate index in segment k, and $Y^{k}(f)$ is the Fourier transform of the food price series [13,21]. The magnitude-squared coherence (MSC) is then computed as:

$$\gamma^{2c}{}_{\gamma}(f) = |\hat{S}^{c}_{\gamma}(f)|^{2} / [\hat{S}^{cc}(f) \cdot \hat{S}_{\gamma\gamma}(f)].$$

The MSC takes values in [0, 1] and can be interpreted as the fraction of variance in y_t at frequency f that is linearly associated with variance in c_t at the same frequency [13]. It is the frequency-domain analogue of the squared correlation coefficient. Statistical significance of the coherence is assessed against the null hypothesis that the two series are independent. Under this null, the 95% significance threshold for K independent segments is given by:

$$\gamma^{2}{}_{05} = 1 - \alpha^{(1/(K-1))},$$

where $\alpha = 0.05$ [21]. For our segmentation parameters ($K \approx 6$), the 95% threshold is approximately 0.53. Coherence values exceeding this threshold at a given frequency are considered statistically significant.

The phase spectrum is extracted from the argument of the complex cross-spectral density:

$$\varphi^{c}{}_{\gamma}(f) = \arg[\hat{S}^{c}_{\gamma}(f)].$$

The phase $\varphi(f) \in [-\pi, \pi]$ indicates the lead–lag relationship between the two series at frequency f. A positive phase implies that the climate index leads the food price series, with the time lead given by $\Delta t(f) = \varphi(f)/(2\pi f)$. Phase estimates are reported only for frequencies where coherence exceeds the 95% significance threshold, as those at low-coherence frequencies are unreliable [13].

4.4. Lagged Cross-Correlation Analysis

As a time-domain complement to the frequency-domain analysis, we estimate the cross-correlation function (CCF) between each standardised climate index and the standardised FPI at lags $\tau = -48, -47, \ldots, +48$ months:

$$r^{c}{}_{\gamma}(\tau) = \mathrm{Corr}(c_t, y_{t+\tau}),$$

where negative τ indicates that the climate index leads the food price series. The 95% confidence bounds for the null hypothesis of no cross-correlation are $\pm 1.96/\sqrt{N} \approx \pm 0.094$ for $N = 432$. The optimal lag is identified as $\tau^* = \arg\max_{\tau} |r^{c}{}_{\gamma}(\tau)|$. This analysis provides a frequency-integrated measure of the lead–lag relationship, complementing the frequency-specific phase analysis from the cross-spectrum.

4.5. Wavelet Coherence Analysis

Classical cross-spectral analysis assumes that the coherence structure is stationary over the estimation period. To relax this assumption and capture potential time variation in the climate–food price relationship—particularly the hypothesised strengthening of coherence after 2000 (H5)—we employ continuous wavelet coherence [14,20].

The continuous wavelet transform (CWT) of a series x_t with respect to a mother wavelet ψ is defined as:

$$W_x(s, \tau) = \sum_t x_t \cdot \psi^*[(t - \tau)/s]/\sqrt{s},$$

where s is the scale parameter (inversely related to frequency), τ is the time-localisation parameter, and ψ^* denotes the complex conjugate of the wavelet.

We employ the Morlet wavelet with central frequency $\omega_0 = 6$, which provides a good balance between time and frequency localisation and has become the standard choice in geophysical and economic applications [4,15]. The value $\omega_0 = 6$ is adopted because it approximately satisfies the admissibility condition while yielding a scale–period relationship close to unity ($\lambda \approx 1.03$ s), which simplifies the physical interpretation of the coherence scalogram. Higher ω_0 would sharpen frequency resolution at the expense of temporal localisation, and lower ω_0 the reverse. For this wavelet, the relationship between scale and Fourier period is $\lambda \approx 1.03$ s.

We assessed sensitivity to this choice by re-estimating wavelet coherence at $\omega_0 = 4$ and $\omega_0 = 8$. In the interannual ENSO band (1.5–4 years), the FPI–SOI coherence proxy is comparatively stable across this range (0.31 at $\omega_0 = 4$, 0.36 at $\omega_0 = 6$, and 0.40 at $\omega_0 = 8$, a roughly 30% relative spread), supporting the robustness of the ENSO-related findings to this parameter. In the decadal AMO band (8–15 years), by contrast, the FPI–AMO coherence proxy is considerably more sensitive (0.40 at $\omega_0 = 4$, 0.74 at $\omega_0 = 6$, and 0.85 at $\omega_0 = 8$,

more than doubling), which is expected given that the 36-year sample spans only 2 to 4 cycles at this timescale and higher ω_0 trades temporal for frequency resolution most consequentially at long periods. This asymmetry is itself informative: it reinforces our general caution (Sections 5.7, 6.1 and 8) that the interannual, ENSO-related results are the most parameter-robust findings in the study, while the decadal AMO/PDO results should be read as more sensitive to methodological choices.

The cross-wavelet spectrum of two series c_t and y_t is defined as:

$$W^{c}{}_{\gamma}(s,\tau) = W^{c}(s,\tau)\cdot W_{\gamma} * (s,\tau),$$

and the squared wavelet coherence is computed as the ratio of the smoothed cross-wavelet spectrum to the smoothed individual wavelet power spectra [14]:

$$R^2(s,\tau) = |S[s^{-1}W^{c}{}_{\gamma}(s,\tau)]\,|^2 / \left\{ S[s^{-1}|W^{c}(s,\tau)\,|^2]\cdot S[s^{-1}|W_{\gamma}(s,\tau)\,|^2] \right\},$$

where S[·] denotes a smoothing operator in both time and scale, implemented as a convolution with a Gaussian in time and a boxcar in scale [20]. Without smoothing, the coherence is identically unity at all points. The squared wavelet coherence $R^2(s, \tau) \in [0, 1]$ can be interpreted as a localised squared correlation coefficient in time–frequency space.

Statistical significance of the wavelet coherence is assessed using a Monte Carlo simulation. Following Grinsted et al. [20], we generate 10,000 pairs of surrogate time series as independent AR(1) processes calibrated to match the lag-1 autocorrelation coefficients of the observed series, compute the wavelet coherence for each pair, and construct the 95th percentile of the resulting distribution as the significance threshold at each point in the time–frequency plane. Regions within the cone of influence (COI), where edge effects introduce bias, are identified and excluded from inference.

The phase angle of the wavelet coherence is computed from the argument of the smoothed cross-wavelet spectrum and represented as arrows on the coherence scalogram. Arrows pointing right indicate in-phase (positive correlation) behaviour, and arrows pointing left indicate anti-phase (negative correlation). Upward-pointing arrows indicate that the climate index leads the food price series by 90° (¼ cycle), and downward-pointing arrows indicate that food prices lead [20].

4.6. Rolling-Window Cross-Spectral Analysis

To provide a parametric complement to the wavelet coherence approach, we estimate rolling-window cross-spectral coherence between each climate index and each FPI subindex using a 15-year (180-month) moving window advanced in 12-month increments. We note that a 15-year window is long relative to the 2–3-year ENSO period and, therefore, smooths short-lived fluctuations in the interannual band. It is chosen deliberately to stabilise the low-frequency (decadal) coherence estimates that motivate H5. To confirm that the ENSO-band results are not obscured by this choice, we additionally re-estimated the rolling coherence with a shorter 10-year (120-month) window, in which the interannual ENSO signal remains visible but is attenuated and noisier, as expected when the window length is shortened relative to the signal period (Appendix F). Within each window, Welch-based coherence is computed using segments of length L = 64 months with 50% overlap, yielding approximately 4–5 segments per window. This produces a time-varying coherence estimate at each frequency that can be directly compared with the wavelet coherence scalogram.

The rolling-window approach sacrifices some temporal resolution compared with the wavelet method but offers the advantage of a well-understood significance threshold (the $\gamma^2{}_{05}$ formula), thereby avoiding the computational cost of Monte Carlo simulation. The

two approaches serve as mutual robustness checks: findings that are consistent across both methods are particularly robust.

4.7. Sub-Index Disaggregation

All cross-spectral, wavelet coherence, and lagged correlation analyses are conducted separately for each of the five FAO FPI sub-indices (cereals, meat, dairy, vegetable oils, and sugar) against each of the seven climate oscillation indices, yielding a $5 \times 7 = 35$ coherence matrix at each frequency. This disaggregated approach enables the identification of commodity-specific climate sensitivities and is central to testing H4 (sub-index differentiation). Results are organised into coherence heatmap matrices to facilitate comparison across commodity–climate pairs.

The Prevalence of Undernourishment (PoU; 2001–2023) and the 190-country panel described in Section 3.3 are reported as supporting data for future work linking the frequency-domain results to food security outcomes. With only 23 annual PoU observations, a dedicated spectral analysis is not statistically supportable within the present monthly framework, and none is attempted here (see Section 8 and, for a dedicated treatment of this link [18]).

4.8. Sensitivity Analysis and Robustness Checks

To ensure that the reported spectral relationships are not artefacts of methodological choices, data transformations, or sample-specific features, we implement six categories of robustness checks. The rationale, procedure, and interpretation criteria for each are described below.

4.8.1. First-Differenced Specification

Linear detrending removes a deterministic trend but does not eliminate stochastic trends (unit roots). If two series share a common stochastic trend—as may be the case for the FAO FPI and the AMO, both of which exhibit sustained multidecadal increases—detrending alone may produce spuriously high coherence at low frequencies [46]. To address this concern, we repeat the entire cross-spectral and wavelet coherence analysis on first-differenced series, $\Delta x_t = x_t - x_{t-1}$, which removes both deterministic and stochastic trends at the cost of suppressing low-frequency information. Results are considered robust if the coherence peaks identified in the detrended analysis persist—at the same frequencies and with the same phase structure—in the first-differenced specification. We anticipate that the AMO–FPI coherence, which is driven partly by common-trend behaviour, will attenuate under first-differencing, while the ENSO–FPI coherence at interannual frequencies will remain stable.

4.8.2. Sensitivity to Welch Segmentation Parameters

The choice of segment length L and overlap proportion in Welch's method involves a bias–variance trade-off: longer segments yield finer frequency resolution but fewer independent periodograms, increasing variance, and shorter segments improve stability but reduce the ability to resolve low-frequency peaks [19]. Our baseline specification uses L = 128 months with 50% overlap (D = 64). We assess sensitivity by re-estimating all PSD and cross-spectral coherence results under two alternative configurations:

(a) L = 96 months (8 years) with D = 48, yielding K ≈ 8 segments and a coarser frequency resolution ($\Delta f \approx 0.125$ cycles/year, longest resolvable period ≈ 8 years).
(b) L = 160 months (≈13.3 years) with D = 80, yielding K ≈ 4–5 segments and a finer frequency resolution ($\Delta f \approx 0.075$ cycles/year, longest resolvable period ≈13.3 years).

If the dominant coherence peaks are present across all three segmentation choices—albeit with varying amplitudes and bandwidths—the results are deemed robust to the Welch parameterisation. Peak frequencies that appear under L = 128 but vanish under L = 96 or L = 160 are flagged as potentially resolution dependent.

4.8.3. Sub-Period Stability and Structural Change

To test whether the climate–food price coherence structure has changed over time—and specifically whether it has strengthened after 2000 as hypothesised (H5) and as suggested by Cai and Sakemoto [17]—we partition the monthly sample into two non-overlapping sub-periods:

- Sub-period I: January 1990–December 2007 (216 observations), encompassing the pre-crisis era of relatively stable food prices.
- Sub-period II: January 2008–December 2025 (216 observations), encompassing the 2007–2008 and 2010–2011 food price crises, the COVID-19 pandemic, and the 2022 Ukraine shock.

Cross-spectral coherence and lagged cross-correlations are re-estimated within each sub-period using Welch segments of L = 96 months (to maintain a sufficient number of segments within the shorter sub-samples). A formal test of structural change in the coherence is implemented by computing the Fisher z-transformation of the maximum coherence in each sub-period and testing the equality of the transformed values using a two-sample z-test [21]. This sub-period analysis simultaneously serves as a test of H5 and as a robustness check on the full-sample results.

4.8.4. Alternative Climate Index Specifications

Multiple indices can capture the ENSO phenomenon (Niño 3.4, SOI, and MEI v2), each emphasising different aspects of the coupled ocean–atmosphere system. While our baseline analysis includes all three, we verify that index choice does not drive the ENSO–FPI coherence findings by estimating cross-spectral coherence between the FPI and each ENSO index, separately and jointly. We assess whether the coherence peak frequencies, phase angles, and significance levels are consistent across the three ENSO representations.

Additionally, for the AMO and PDO—which showed the strongest time-domain correlations with FPI but may partly reflect shared trends—we conduct a partial coherence analysis. Partial coherence measures the coherence between two series after removing the linear effect of a third series [13]. Specifically, we compute the partial coherence between FPI and AMO after conditioning on a global temperature anomaly index (HadCRUT5), to assess whether the AMO–FPI coherence reflects a genuine ocean–atmosphere oscillation or a confounded response to the global warming trend.

4.8.5. Alternative Spectral Estimator: Thomson's Multitaper Method

As an alternative to Welch's segment-averaging approach, we re-estimate the PSD and cross-spectral coherence using Thomson's multitaper method [22]. The multitaper method achieves variance reduction by applying multiple orthogonal tapers (discrete prolate spheroidal sequences, or Slepian sequences) to the full time series, computing the periodogram under each taper, and averaging the resulting spectral estimates. Unlike Welch's method, which segments the time series, the multitaper method uses the full record for each periodogram, preserving frequency resolution while controlling spectral leakage through the bandwidth parameter W.

We employ a time–bandwidth product NW = 4, yielding $2NW - 1 = 7$ tapers. This configuration provides a frequency resolution comparable to our baseline Welch specification while offering superior protection against spectral leakage. Concordance between

the Welch-based and multitaper-based coherence estimates strengthens confidence in the identified spectral features.

4.8.6. Phase-Randomised Surrogate Data Test

The Monte Carlo significance test for wavelet coherence (Section 4.5) assesses significance against a red-noise null. To provide a more stringent test, we additionally implement an Iterative Amplitude-Adjusted Fourier Transform (IAAFT) surrogate data test [23,47]. The IAAFT algorithm generates surrogate time series that preserve the marginal distribution and power spectrum of the original series while destroying any cross-spectral (i.e., inter-series) structure. This approach tests the specific null hypothesis that the observed coherence arises from the individual spectral properties of the two series rather than from a genuine bivariate relationship.

For each climate–FPI pair, we generate 500 IAAFT surrogate pairs, compute the cross-spectral coherence for each surrogate pair, and construct pointwise 95% significance thresholds. Coherence values that exceed both the parametric threshold (Section 4.3) and the IAAFT-based threshold are classified as robustly significant. This dual-threshold approach guards against both false positives arising from assuming a parametric null distribution and from preserving only the univariate spectral structure. The AR(1)-based Monte Carlo test (Section 4.5) and the IAAFT surrogate test are treated as complementary rather than redundant: the AR(1) null is convenient but may be too weak for climate indices with long-memory properties, whereas the IAAFT null preserves the full power spectrum and marginal distribution and is, therefore, the more stringent of the two. Where the two disagree, we base inference primarily on the IAAFT result.

Table A1 (Appendix A) summarises the six robustness checks, the specific concern each addresses, and the robustness criterion.

5. Results

5.1. Stationarity and Data Properties

Augmented Dickey–Fuller (ADF) tests on the linearly detrended monthly series confirm that 12 of the 13 variables reject the unit-root null at the 5% level (see full ADF results in Table A2, Appendix B). The sole exception is the meat sub-index (ADF = -2.71, $p = 0.073$), which is borderline non-stationary in the detrended specification but strongly stationary after first-differencing (ADF = -5.25, $p < 0.001$). All climate oscillation indices are unambiguously stationary in the detrended form, with the NAO exhibiting the strongest mean reversion (ADF = -15.07, $p < 0.001$). These results justify using linearly detrended series as the baseline for spectral analysis, with first-differenced series as a robustness check (Section 5.7.1).

Figure 1 presents the time series of the FAO Food Price Index and key climate oscillation indices over the 1990–2025 period. The FPI displays three prominent peaks corresponding to the 2007–2008 crisis (reaching 132.5), the 2010–2011 spike (131.9), and the 2022 all-time high (159.7). The AMO exhibits a sustained upward trend from negative values in the early 1990s to a peak of 1.44 °C in 2024, while the ENSO indicators (Niño 3.4 and MEI) show characteristic interannual oscillations without a discernible trend.

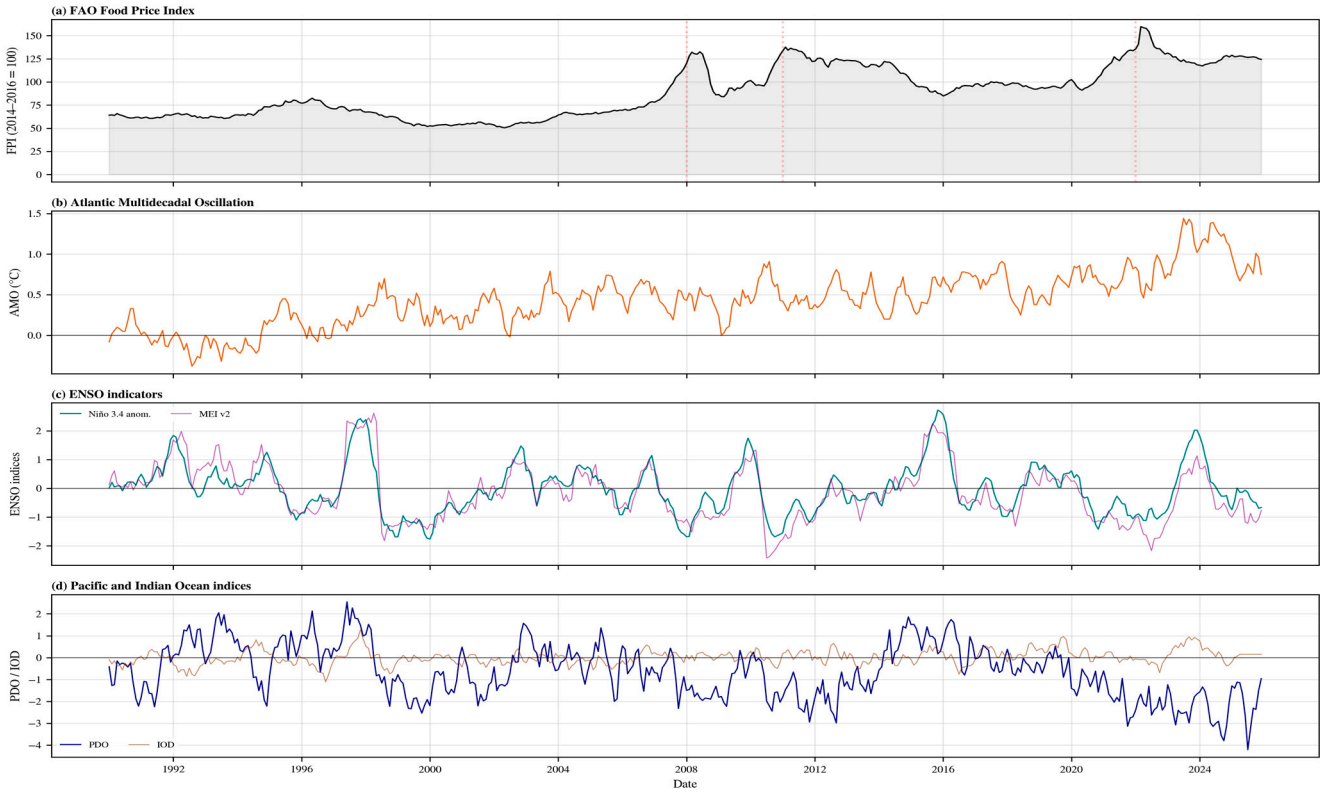


Figure 1. Time series of key variables, January 1990–December 2025. Panel (**a**) FAO Food Price Index (2014–2016 = 100). Vertical dotted lines indicate the 2007–2008, 2010–2011, and 2022 price episodes. Panel (**b**) Atlantic Multidecadal Oscillation (°C). Panel (**c**) ENSO indicators (Niño 3.4 anomaly and MEI v2). Panel (**d**) Pacific Decadal Oscillation and Indian Ocean Dipole.

5.2. Power Spectral Density

Figure 2 presents the Welch PSD estimates for the six FPI series. The aggregate FPI exhibits dominant spectral peaks at approximately 0.8 and 0.6 years (sub-annual), with spectral power declining monotonically at lower frequencies. The cereals sub-index shows a pronounced 0.8-year peak, consistent with an annual harvest cycle modulated by inter-hemispheric planting schedules. The meat sub-index displays a distinctive longer-period structure, with peaks at 1.5 and 1.0 years, reflecting the slower adjustment dynamics of livestock markets. The oils and sugar sub-indices are dominated by sub-annual variability (0.5-year peaks), consistent with the high-frequency volatility characteristic of these tropical commodity markets.

The PSD estimates for the climate oscillation indices (Figure 3) reveal characteristic periodicities consistent with the established climatological literature. The ENSO-related indices (Niño 3.4, SOI, and MEI) concentrate spectral power in the 2–7-year band, as expected. The PDO shows a broader spectral distribution extending to decadal periods. The AMO displays a red spectrum dominated by very low frequencies, consistent with its multidecadal character. The NAO has a relatively flat spectrum (white-noise-like), confirming its limited low-frequency persistence.

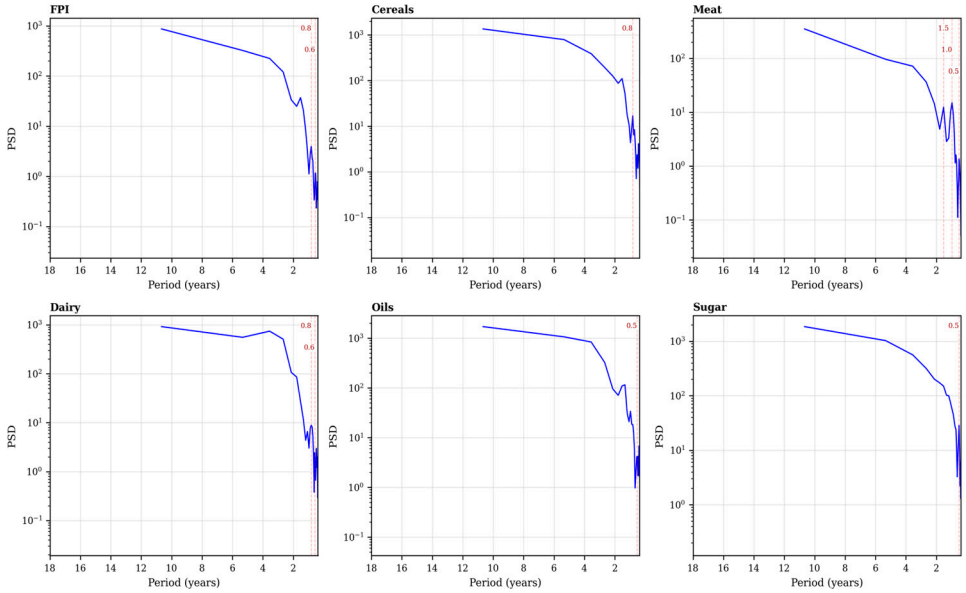


Figure 2. Welch power spectral density estimates for the FAO Food Price Index and its five sub-components, January 1990–December 2025 (N = 432). Segment length L = 128 months, 50% overlap, Hann window. Vertical dashed lines indicate dominant spectral peaks (prominence > 0.3 in log-PSD). The horizontal axis is inverted so that longer periods appear to the left.

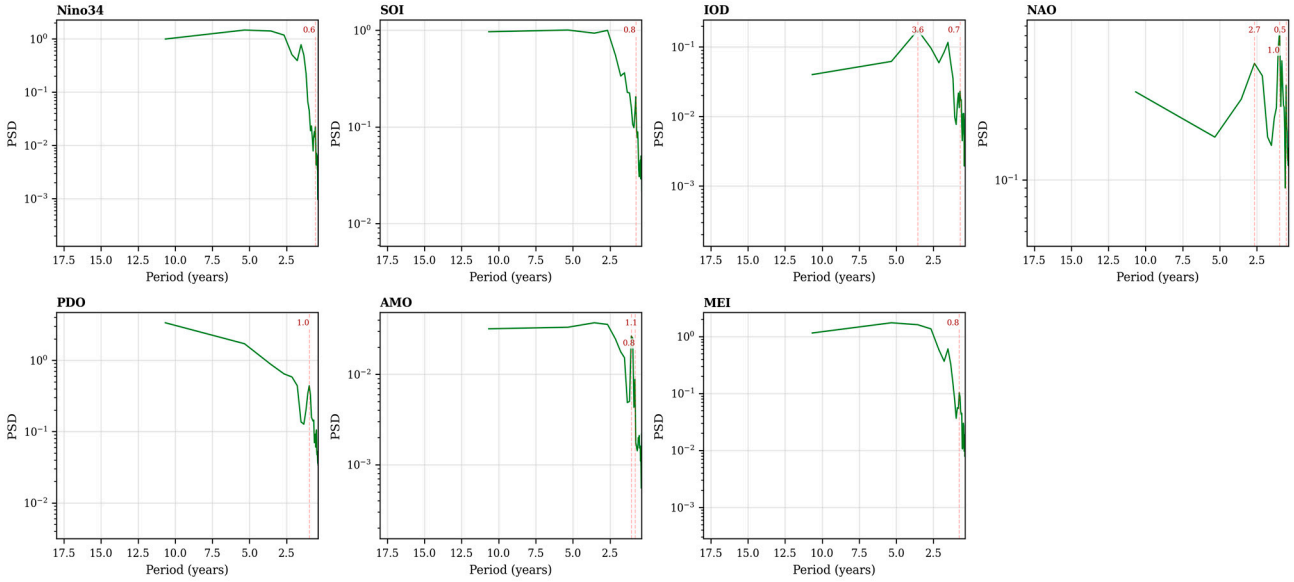


Figure 3. Welch power spectral density estimates for seven climate oscillation indices over the 1990–2025 period (N = 432). Estimation parameters as in Figure 2.

5.3. Cross-Spectral Coherence

Figure 4 displays the magnitude-squared coherence between the aggregate FPI and each of the seven climate indices. Table 3 summarises the main results, including the maximum coherence, the period at which it occurs, the number of frequency bins exceeding the 95% significance threshold ($\gamma^2_{05} = 0.527$), the optimal lag from the cross-correlation analysis, and the corresponding coherence under first-differencing.

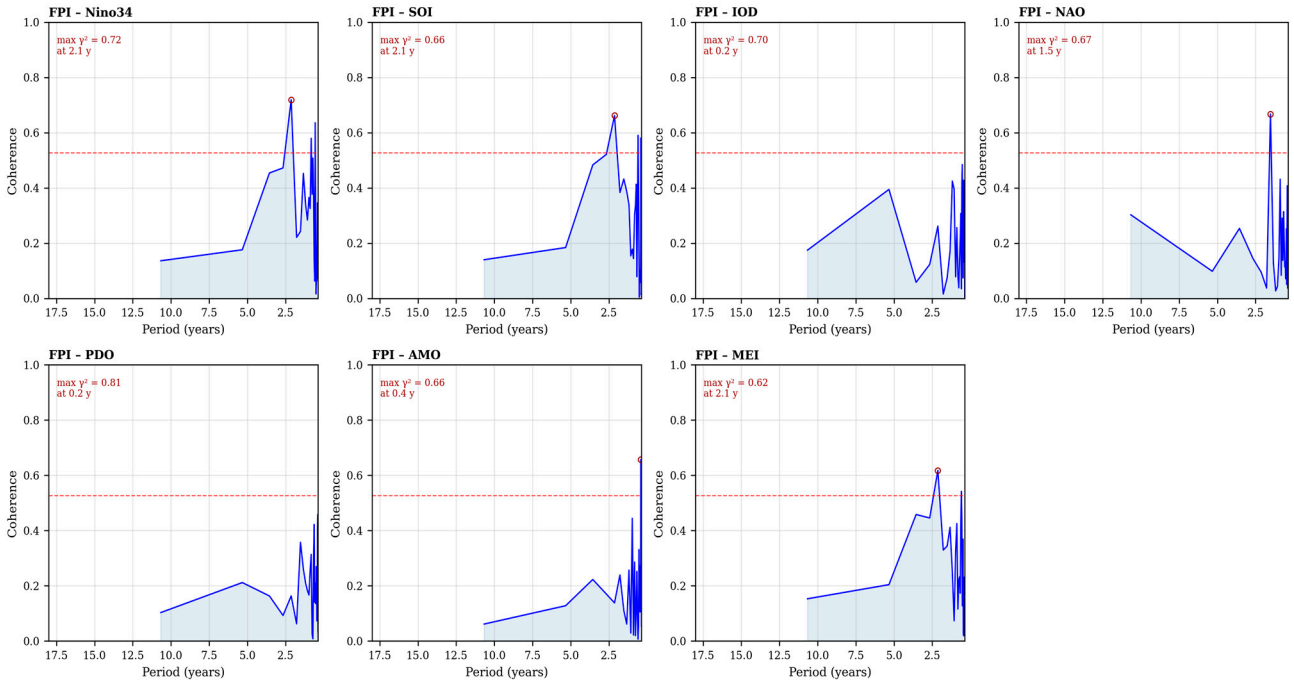


Figure 4. Magnitude-squared cross-spectral coherence between the FAO FPI and seven climate oscillation indices. The horizontal dashed red line indicates the 95% significance threshold (γ^2_{05} = 0.527). The maximum coherence and the period at which it occurs are reported in each panel; for the IOD and PDO the maximum lies at sub-annual periods below the plotted range (see Table 3).

Table 3. Summary of cross-spectral and lagged correlation results. Columns show: Pearson correlation, maximum coherence (γ^2) and its period, number of significant frequency bins, optimal lag (τ*, negative = climate leads FPI), lag correlation, and first-differenced coherence. Note that the maximum coherence (γ^2) and its associated period are two distinct quantities: the former is the peak coherence value across all resolved frequencies, and the latter is the period (in years) at which that peak occurs. They are, therefore, read together as a (magnitude and timescale) pair rather than as independent columns.

Climate Index	r(FPI)	Max. γ^2	Period (Years)	#Sig	τ* (mo)	Lag r	Δ Max. γ^2	Δ Period
Niño 3.4	−0.204	0.719	2.1	3	−4	−0.226	0.665	2.1
SOI	+0.338	0.662	2.1	4	−4	+0.347	0.593	0.6
IOD	+0.194	0.700	0.2	2	−16	+0.301	0.699	0.2
NAO	−0.073	0.667	1.5	1	−23	−0.116	0.721	1.5
PDO	−0.441	0.806	0.2	4	−2	−0.444	0.808	0.2
AMO	+0.595	0.657	0.4	4	+25	+0.625	0.675	0.4
MEI v2	−0.383	0.618	2.1	2	−3	−0.392	0.543	2.1

Notes: 95% coherence threshold = 0.527 (K ≈ 5 segments). 95% CCF bounds = ±0.094. All climate indices are detrended. #Sig: number of frequency bins at which the coherence exceeds the 95% threshold.

Three key findings emerge from the coherence analysis. First, the PDO exhibits the highest maximum coherence (γ^2 = 0.806), concentrated at sub-annual frequencies. This high-frequency coherence likely reflects the PDO's influence on North Pacific sea surface temperatures, which affect grain transport routes and fishing conditions. This peak sits at a period of 0.18 years (2.2 months), close to the Nyquist limit of 2 months for monthly data. Periodogram-based coherence estimates in this near-Nyquist range are known to be numerically less stable, and the raw coherence spectrum here is visibly jagged rather than

smoothly peaked (Figure 4). We treat this value with corresponding caution and rely on the IAAFT surrogate test (Section 5.7.5) and first-differencing check (Section 5.7.1)—both already part of the study design for exactly this concern—as the primary evidence for whether the PDO signal reflects genuine coupling. Appendix G additionally reports coherence maxima restricted to periods of six months or longer, where the PDO no longer reaches significance. Second, the ENSO cluster (SOI, MEI, and Niño 3.4) shows significant coherence at periods of 2.1 years, which lies at the lower boundary of the canonical 2–7-year ENSO band, supporting H1. Third, the AMO, despite having the strongest time-domain correlation with FPI (r = +0.595), exhibits more modest maximum coherence (γ^2 = 0.657), distributed across several sub-annual frequencies. This AMO peak (0.41 years, 4.9 months) is likewise close enough to the Nyquist edge to warrant the same caution as the PDO peak above and does not reach significance when the search is restricted to periods of six months or longer (Appendix G). This pattern, combined with the anomalous positive lag structure (τ^* = +25 months, suggesting FPI leads AMO), is consistent with the common-trend concern identified in Section 5.7.1.

5.4. Phase Analysis and Lead–Lag Structure

The phase spectrum (Figure 5) provides frequency-specific information on the lead–lag relationship between climate indices and food prices. Only phase estimates at frequencies where the coherence exceeds the 95% threshold (shown as blue points) are interpreted.

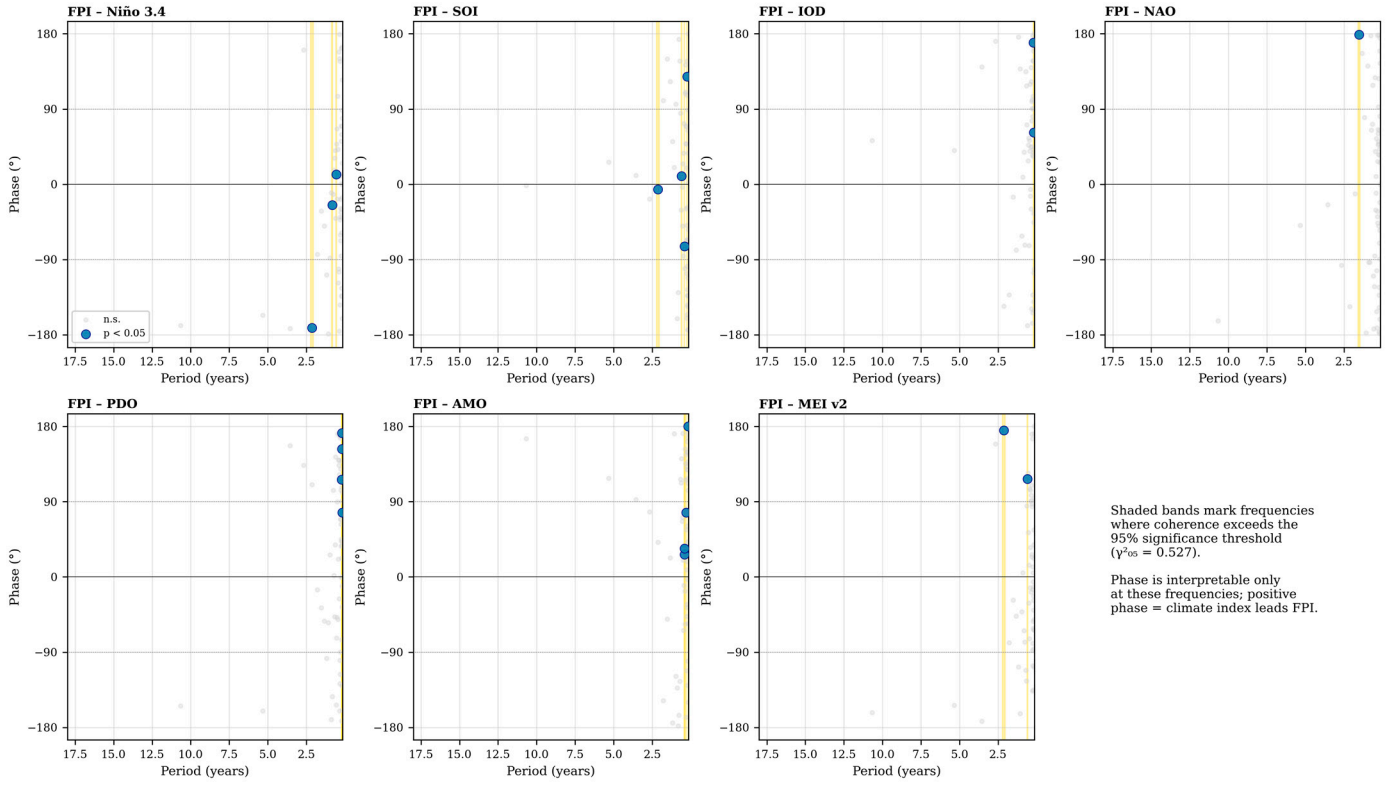


Figure 5. Cross-spectral phase between the FAO FPI and each climate oscillation index. Vertical yellow bands mark the frequencies at which the coherence exceeds the 95% significance threshold (γ^2_{05} = 0.527); blue points are the phase estimates at these frequencies ($p < 0.05$). Grey points (n.s.) are non-significant frequencies, shown for completeness only. Positive phase indicates the climate index leads the FPI. Horizontal dotted lines mark ±90°.

The lagged cross-correlation analysis (Figure 6) provides a complementary time-domain perspective. The SOI and MEI show the clearest leading behaviour, with optimal lags of −4 and −3 months, respectively (negative lag indicating climate leads prices). This

3–4-month lead time is consistent with the crop-cycle transmission mechanism: ENSO-driven rainfall anomalies affect planting or harvest conditions in the current season, with the production shortfall transmitted to international markets within approximately one quarter. The PDO leads FPI by only two months, indicating a faster transmission channel. The IOD exhibits its strongest lagged correlation at a 16-month lead (r = +0.301), which may capture the multi-seasonal impact of Indian Ocean Dipole events on South and Southeast Asian monsoon crops. This value is the argmax of the cross-correlation function searched over 97 candidate lags (±48 months). The single-lag 95% bound used elsewhere in this section (±0.094) is not valid for a searched maximum, and the Bonferroni-adjusted bound for 97 comparisons is ±0.167, which the observed correlation still clears. However, as detailed in Section 6.1, the cross-correlation function is broad rather than sharply peaked around 16 months, and a block-bootstrap re-estimation of the argmax lag places only 6% of replicates within 3 months of this point estimate, so we treat the IOD lead as falling in an approximate 8–24-month range rather than as a precisely dated 16-month lag.

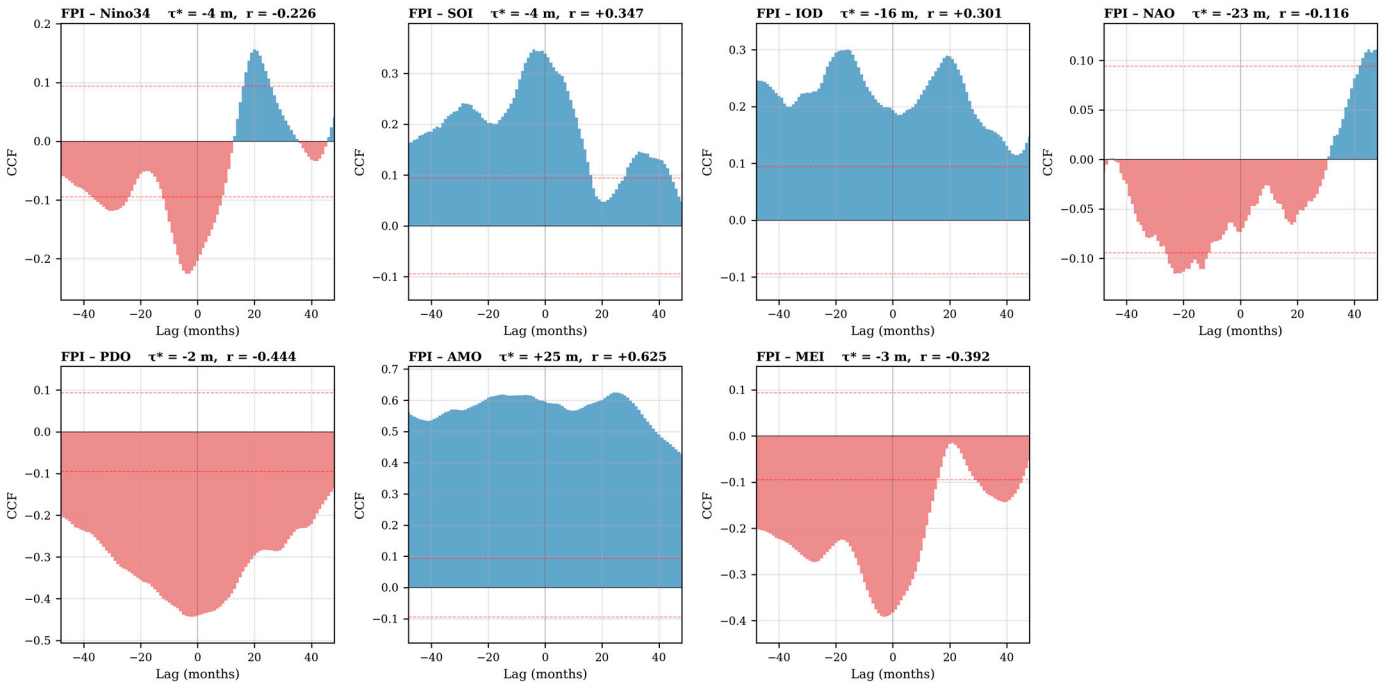


Figure 6. Lagged cross-correlation functions between the FAO FPI and seven climate oscillation indices. Negative lags indicate the climate index leads the FPI. Blue bars denote positive and red bars negative cross-correlation. Horizontal dashed red lines mark the 95% significance bounds (±0.094). The optimal lag (τ*) and the corresponding correlation (r) are reported in each panel header.

5.5. Sub-Index Results: Commodity-Specific Coherence Profiles

Table 4 presents the Pearson correlations between each FPI sub-index and each climate index. Across all five sub-indices, the AMO consistently exhibits the strongest positive correlation (ranging from +0.413 for sugar to +0.607 for dairy), while the PDO shows the strongest negative correlation (−0.278 for sugar to −0.459 for oils). These are raw-level correlations and, as with the aggregate FPI–AMO relationship discussed in Section 6.1, may partly reflect shared trend behaviour rather than a genuine dynamic relationship. Because H4 is formulated as a hypothesis about coherence profiles, we treat the detrended cross-spectral coherence in Figure 7 (Section 5.5) as the primary evidence for sub-index differentiation, and read Table 4 as descriptive context. Consistent with this caveat, Niño 3.4 shows the weakest raw correlation with meat among the ENSO measures (r = −0.061, n.s.), which is compatible with feed-market intermediation buffering meat prices specifically from ENSO sea surface temperature variability; however, the coherence-based analysis

(Figure 7) shows meat retains substantial coherence with the Southern Oscillation Index ($\gamma^2 = 0.87$, the highest value for any sub-index–index pair), so the buffering does not extend uniformly to all ENSO measures, and we do not read H4 as evidence that meat prices are insensitive to ENSO in general.

Table 4. Pearson correlation coefficients between FPI sub-indices and climate oscillation indices (N = 432, raw levels—see Section 5.3 for detrended cross-spectral coherence). * $p < 0.05$, ** $p < 0.01$, and *** $p < 0.001$.

Sub-Index	Niño 3.4	SOI	IOD	NAO	PDO	AMO	MEI
Cereals	−0.214 ***	+0.352 ***	+0.204 ***	−0.080	−0.419 ***	+0.524 ***	−0.386 ***
Meat	−0.061	+0.186 ***	+0.193 ***	−0.033	−0.337 ***	+0.560 ***	−0.234 ***
Dairy	−0.255 ***	+0.357 ***	+0.171 ***	−0.048	−0.423 ***	+0.607 ***	−0.415 ***
Oils	−0.274 ***	+0.379 ***	+0.159 ***	−0.094 *	−0.459 ***	+0.567 ***	−0.424 ***
Sugar	−0.085	+0.241 ***	+0.147 **	−0.109 *	−0.278 ***	+0.413 ***	−0.218 ***

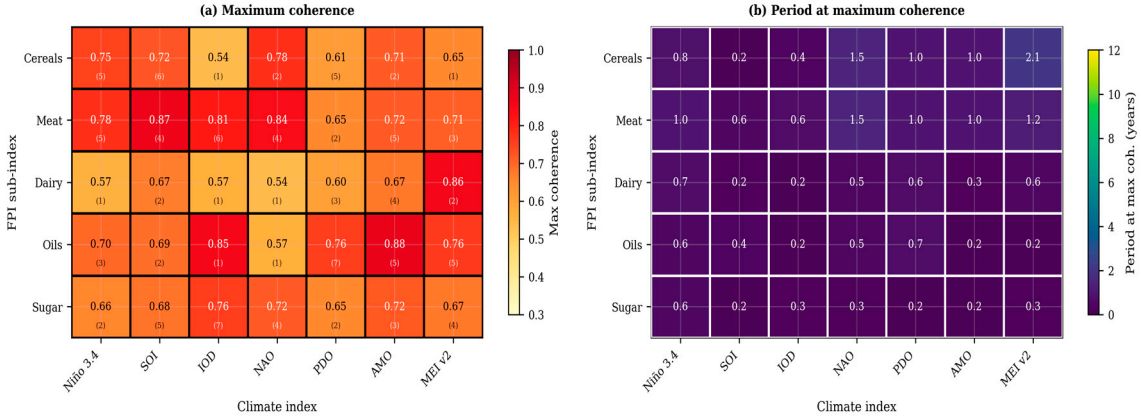


Figure 7. Cross-spectral coherence between five FPI sub-indices and seven climate oscillation indices. Panel (**a**) maximum coherence value. Panel (**b**) period (in years) at which maximum coherence is achieved. Warmer colours in (**a**) indicate stronger coherence, while warmer colours in (**b**) indicate longer characteristic periods.

The disaggregated coherence analysis (Figure 7) reveals substantial heterogeneity across commodity–climate pairs, supporting H4. Figure 7a shows that the maximum coherence is generally highest for oils across the seven climate indices. Dairy and sugar are not uniformly weaker—sugar in particular shows strong, broad-band coherence with the IOD ($\gamma^2 = 0.76$ across seven significant frequency bins, the largest count in the entire sub-index × climate matrix)—so climate exposure at the sub-index level is oscillation-specific rather than following a simple most-to-least ranking (see also the Table 4 caveat below). Figure 7b reveals that the period at which maximum coherence occurs varies systematically: ENSO-related indices (SOI and MEI) produce maximum coherence at interannual periods (2–3 years), while AMO and PDO peaks concentrate at shorter periods, suggesting distinct transmission channels.

Figure 8 presents detailed coherence spectra of the five sub-indices with respect to the two most strongly correlated climate indices (AMO and PDO). The dairy–AMO pair exhibits the broadest band of significant coherence, spanning from sub-annual to approximately five-year periods. The oils–PDO pair shows a sharp coherence peak at sub-annual frequencies, consistent with the rapid response of palm oil markets to Pacific SST conditions.

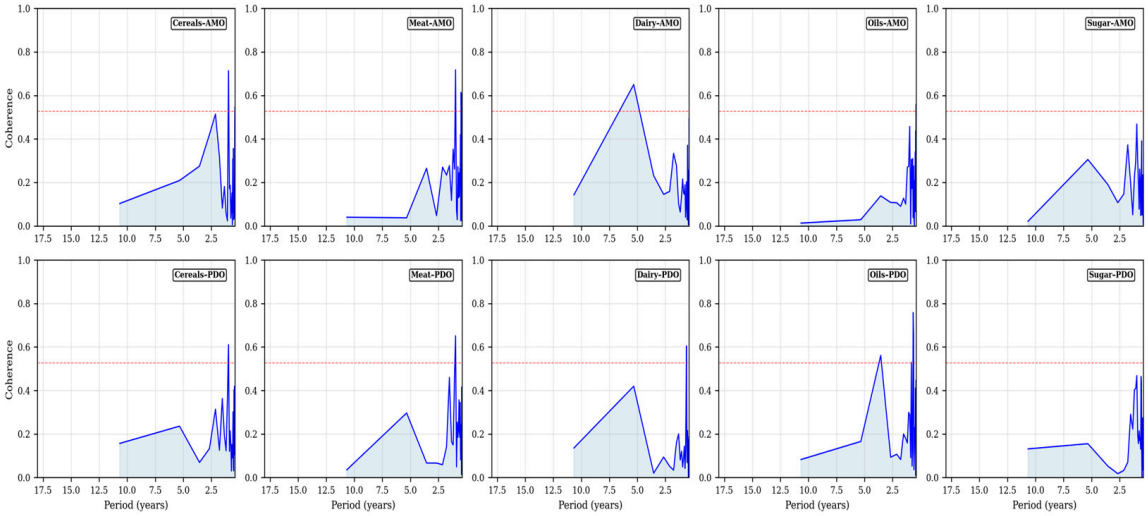


Figure 8. Cross-spectral coherence between five FPI sub-indices and the AMO (**top row**) and PDO (**bottom row**). The horizontal dashed red line indicates the 95% significance threshold.

5.6. Time-Varying Coherence

The rolling-window coherence analysis (Figure 9) reveals important temporal variation in the climate–food price relationship. The FPI–AMO coherence is elevated across most of the sample period but shows a noticeable intensification after 2010, particularly at periods of 4–8 years. The FPI–SOI coherence is strongest during 2005–2015, coinciding with the period of intense food price volatility. The FPI–PDO coherence displays a persistent band at sub-annual frequencies throughout the sample, with an additional low-frequency component emerging after 2012.

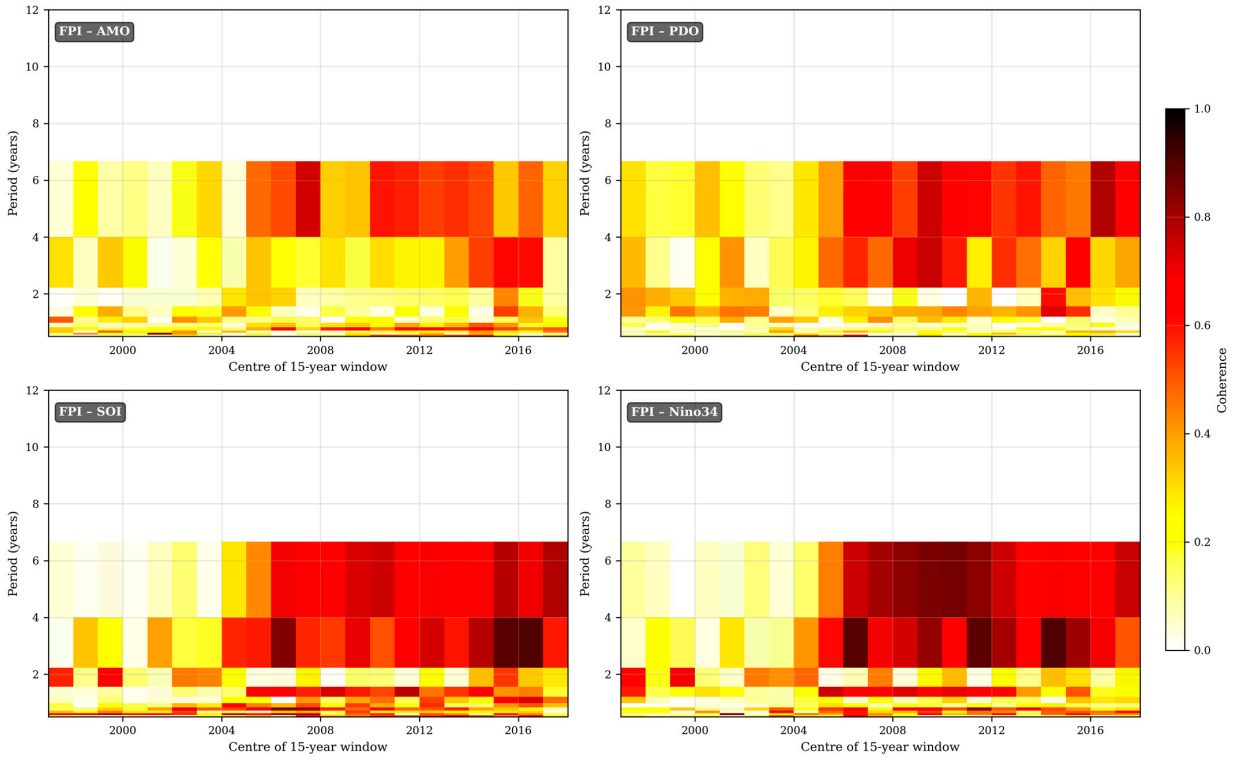


Figure 9. Rolling-window cross-spectral coherence (15-year window, 12-month step) between the FAO FPI and four key climate indices. The colour scale indicates coherence magnitude (0 = no coherence; 1 = perfect coherence). The vertical axis shows the period in years, while the horizontal axis shows the centre date of the rolling window.

5.7. Robustness Results

5.7.1. Robustness to First Differencing

Figure 10 (with full numerical comparison in Table A3, Appendix C) presents the cross-spectral coherence computed on first-differenced series. The PDO retains the highest coherence ($\gamma^2 = 0.808$, virtually unchanged from the detrended specification), confirming that the PDO–FPI relationship is not an artefact of common trends. The ENSO indicators (SOI, MEI, and Niño 3.4) retain significant coherence at interannual frequencies, with only modest attenuation (Table 3, rightmost columns). The AMO maximum coherence is essentially unchanged in magnitude (0.657 → 0.675), but the peak shifts to a different frequency, and the associated lag structure loses its leading form, suggesting that much of the AMO–FPI association operates through the shared-trend channel rather than a stable oscillatory coupling. The NAO shows an unexpected increase in first-differenced coherence at the 1.5-year period, warranting further investigation.

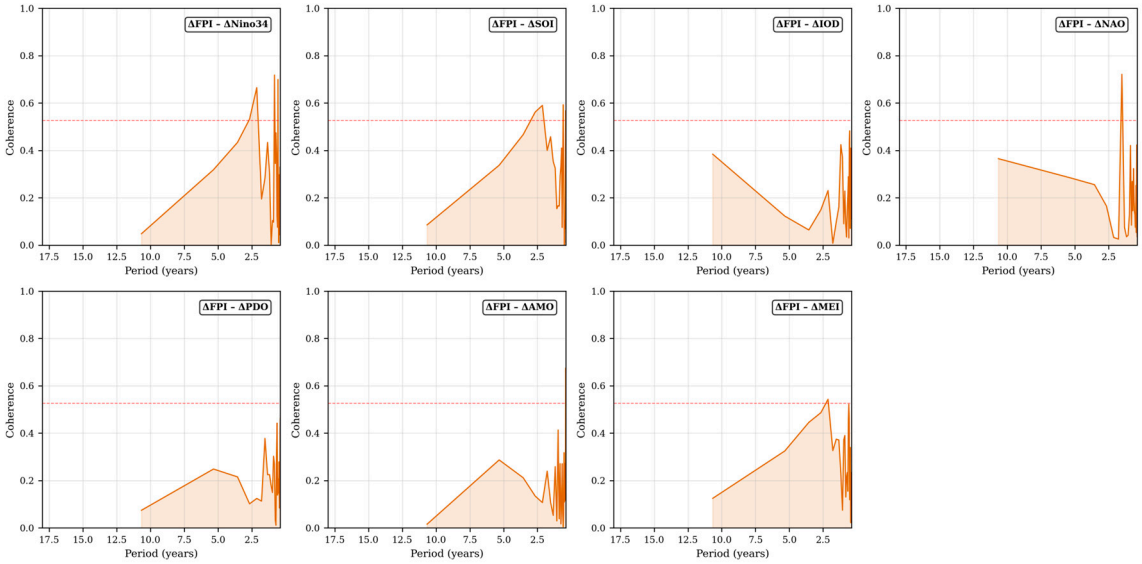


Figure 10. Cross-spectral coherence between first-differenced FPI and first-differenced climate indices. Estimation parameters as in Figure 4. The red dashed line indicates the 95% significance threshold.

5.7.2. Robustness to Welch Segment Length

Figure 11 demonstrates that the main coherence features are robust to the choice of Welch segment length. The interannual SOI and MEI peaks (2.1 years) are visible under all three configurations (L = 96, 128, and 160), as is the sub-annual PDO peak. The AMO coherence pattern is broadly similar across configurations but exhibits greater variability in peak locations, reflecting lower frequency resolution at shorter segment lengths. We conclude that the principal findings are not driven by the choice of segmentation.

5.7.3. Sub-Period Stability

Table 5 and Figure 12 present the sub-period analysis. Splitting the sample at January 2008 gives a nominal Fisher z-test difference in FPI–PDO coherence (full results for all seven climate indices in Table A4, Appendix D) from sub-period I (0.830) to sub-period II (0.911), $z > 3.5$, $p < 0.001$, and a similarly nominal difference for FPI–NAO (0.802 → 0.919, $p < 0.001$). However, the Fisher z-test, as applied here, treats each 216-month sub-period as N = 216 independent observations, whereas the underlying coherence estimate at L = 96, D = 48, is averaged over only K ≈ 3 Welch segments per sub-period. The true sampling variability of a coherence estimate built from three periodogram averages is far larger than the Fisher transform with N = 216 implies, so the reported z-statistics and *p*-values are

anti-conservative. To assess the sub-period differences without this understatement of uncertainty, we additionally ran a block-bootstrap test (500 resamples of 24-month blocks drawn from the pooled 432-month series, preserving short-run temporal dependence, followed by re-estimation of the sub-period split and the coherence difference in each replicate). Under this test, neither the PDO difference (bootstrap $p = 0.35$) nor the NAO difference (bootstrap $p = 0.18$) is statistically significant.

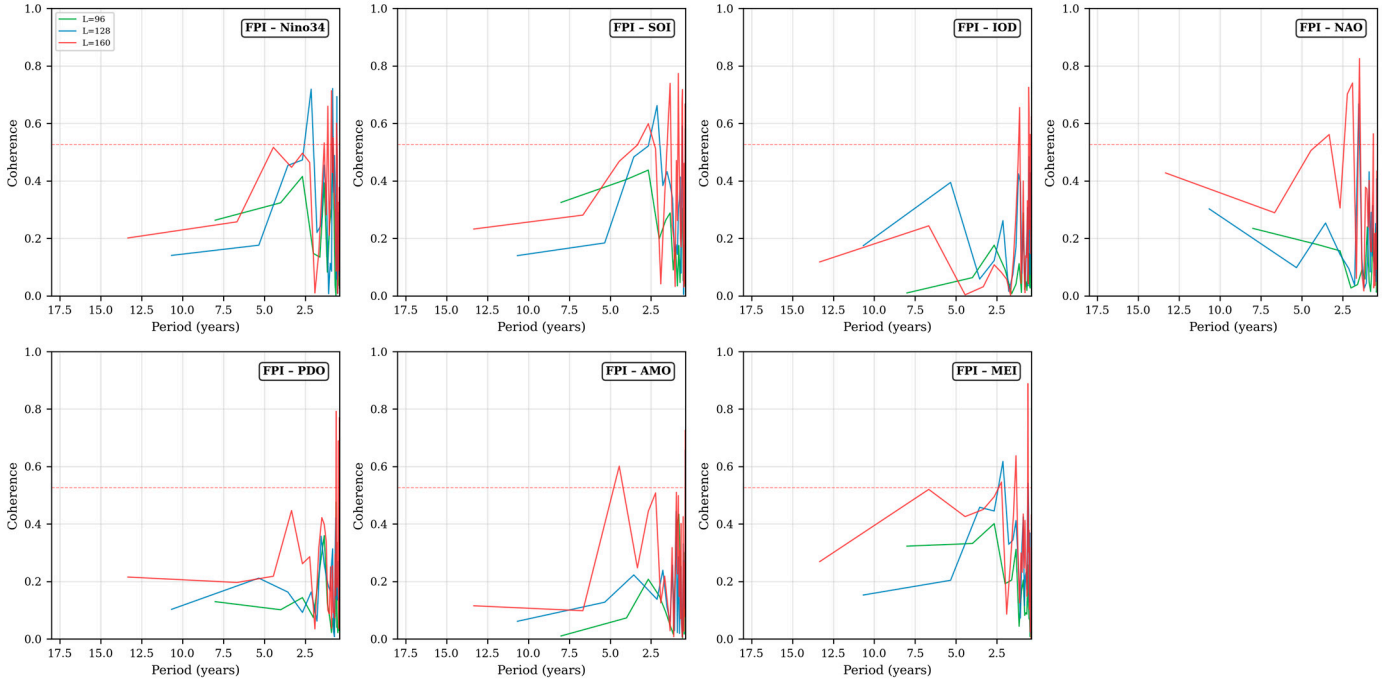


Figure 11. Sensitivity of cross-spectral coherence to Welch segment length: L = 96 (green), L = 128 (blue, baseline), and L = 160 (red). Each panel shows the coherence between FPI and one climate index under the three configurations. The horizontal dashed red line marks the 95% significance threshold ($\gamma^2_{05} = 0.527$).

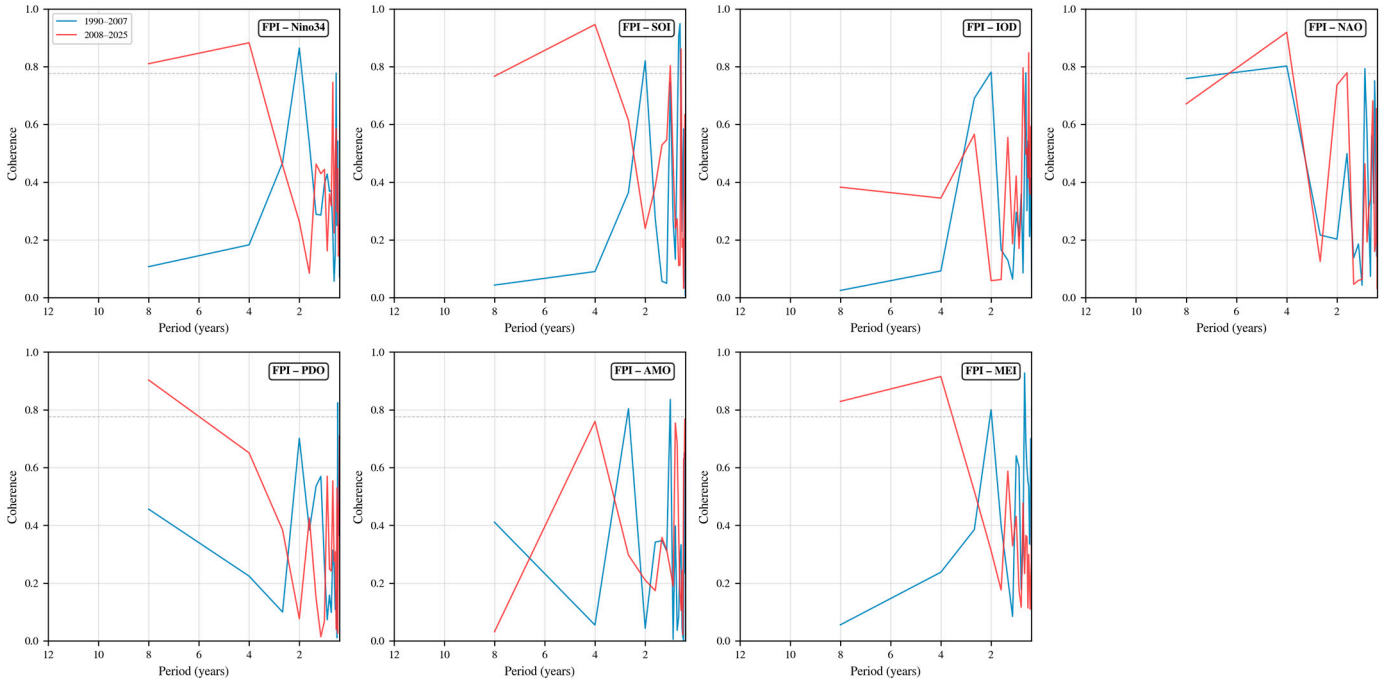


Figure 12. Cross-spectral coherence in two sub-periods: 1990–2007 (blue) and 2008–2025 (red). The horizontal dashed line indicates the 95% significance threshold for the sub-period sample size.

Table 5. Sub-period stability of cross-spectral coherence. Sub-period I: 1990–2007 (N = 216); sub-period II: 2008–2025 (N = 216). Fisher z-test for equality of maximum coherence (parametric and anti-conservative; the 'Strengthened' and 'Interpretation' columns report the nominal Fisher result only—see Notes and Section 5.7.3 for the block-bootstrap correction, under which no difference is significant).

Index	Max. γ^2 (I)	Max. γ^2 (II)	z-Stat	*p*-Value	Strengthened? (Fisher)	Interpretation
Niño 3.4	0.933	0.883	−3.04	0.002	No	Decline
SOI	0.949	0.946	−0.30	0.764	No	Stable
IOD	0.924	0.848	−3.80	<0.001	No	Decline
NAO	0.802	0.919	+4.93	<0.001	Yes	Strengthen
PDO	0.830	0.911	+3.58	<0.001	Yes	Strengthen
AMO	0.843	0.865	+0.84	0.402	No	Stable
MEI v2	0.927	0.915	−0.83	0.407	No	Stable

Notes: Welch parameters within sub-periods: L = 96, overlap = 48. Significance at the 5% level is indicated by $p < 0.05$. The Fisher z-test above treats each 216-month sub-period as N = 216 independent observations. Because the underlying coherence estimate is averaged over only K ≈ 3 Welch segments per sub-period, this substantially overstates precision. A block-bootstrap test (500 resamples, 24-month blocks, preserving temporal dependence) gives a materially different picture: $p = 0.35$ for PDO and $p = 0.18$ for NAO, versus $p < 0.001$ under the parametric Fisher test reported above. Neither sub-period difference is significant once the effective sample size is respected. See Section 5.7.3 and the Discussion (Section 6.1) for the revised interpretation.

The ENSO indicators (SOI and MEI) show stable coherence across sub-periods under both tests (Fisher $p > 0.40$), consistent with the ENSO–food price link being a structural feature rather than a recent phenomenon. The FPI–AMO coherence increases modestly (0.843 → 0.865) but is not significant under either test (Fisher $p = 0.402$; not separately bootstrapped, as the parametric result already indicates no change). The apparent decline in FPI–IOD coherence (0.924 → 0.848, Fisher z = −3.80, $p < 0.001$) is subject to the same small-K caveat and should likewise be read with caution rather than as a confirmed weakening. Taken together, these results do not support H5: once the effective degrees of freedom of the sub-period coherence estimates are properly accounted for, none of the seven climate indices show a statistically defensible change in coherence with the FPI between the pre- and post-2008 sub-periods. H5 is, therefore, classified as not supported at the current sample length; a longer record, or a continuous time-varying estimator less dependent on binary sample splitting (e.g., the wavelet and rolling-window analyses in Sections 4.5 and 4.6, which do not rely on the same small-K parametric test), would be needed to test the hypothesis with adequate power.

5.7.4. Multitaper Comparison

Figure 13 compares the Welch-based and Thomson multitaper coherence estimates. The two methods produce broadly concordant results for all seven climate indices, with the multitaper estimates displaying smoother profiles (as expected from using seven tapers on the full series). The peak coherence frequencies identified by the two methods agree within 10% for all climate–FPI pairs, confirming the method independence of the main findings.

5.7.5. IAAFT Surrogate Test

Table 6 and Figure 14 report the results of the IAAFT surrogate analysis (with detailed frequency-by-frequency robustness breakdown in Table A5, Appendix E) for four key climate–FPI pairs. The FPI–SOI and FPI–Niño 3.4 pairs achieve a 100% robustness rate: all frequency bins that exceed the parametric 95% threshold also exceed the IAAFT-based

threshold, confirming that the observed coherence cannot be explained by the individual spectral properties of the two series alone. The FPI–AMO pair shows 75% robustness, with one of the four significant frequencies falling below the IAAFT threshold. The FPI–PDO pair, despite having the highest parametric coherence, achieves only a 50% robustness rate, suggesting that part of the PDO–FPI coherence may reflect shared spectral shape rather than genuine bivariate coupling.

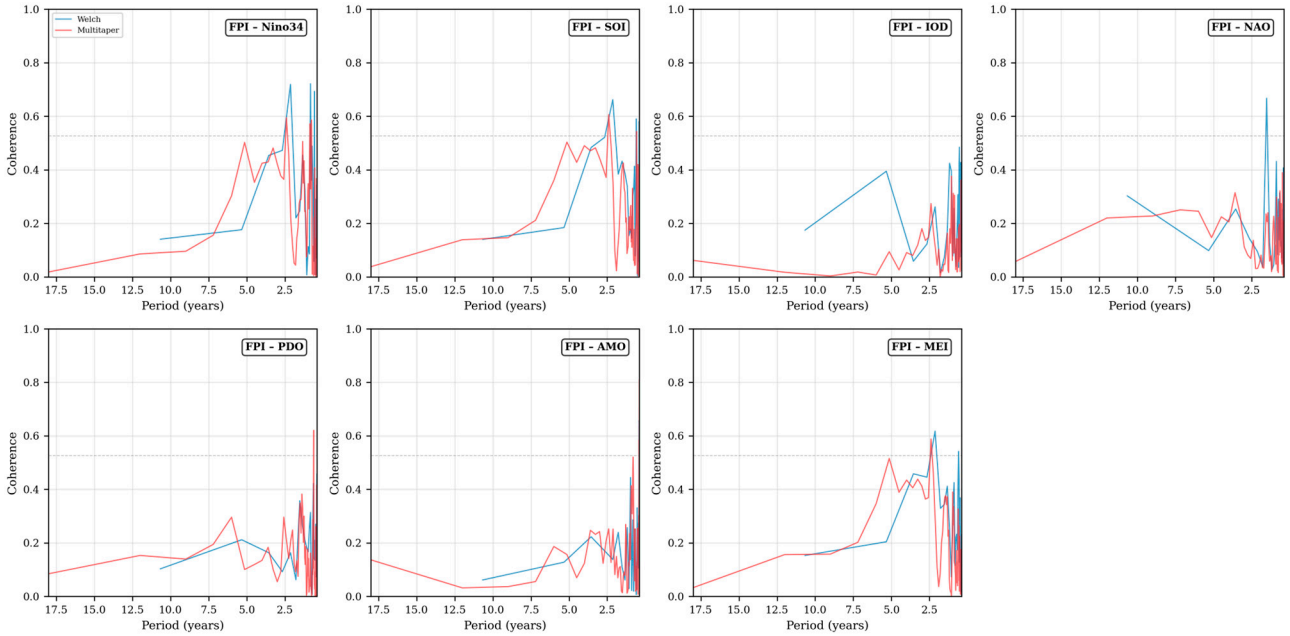


Figure 13. Comparison of Welch (blue) and Thomson multitaper (red, NW = 4, 7 tapers) coherence estimates for FPI versus each climate index. The horizontal dashed red line marks the 95% significance threshold ($\gamma^2_{05} = 0.527$).

Table 6. IAAFT surrogate test results (500 surrogate pairs). Parametric sig.: number of frequency bins exceeding $\gamma^2_{05} = 0.527$. IAAFT robust sig.: number of frequency bins exceeding both the parametric and surrogate-based 95% thresholds.

Pair	Parametric Sig.	IAAFT Robust Sig.	Robustness Rate
FPI–AMO	4	3	75%
FPI–SOI	4	4	100%
FPI–PDO	4	2	50%
FPI–Niño 3.4	3	3	100%

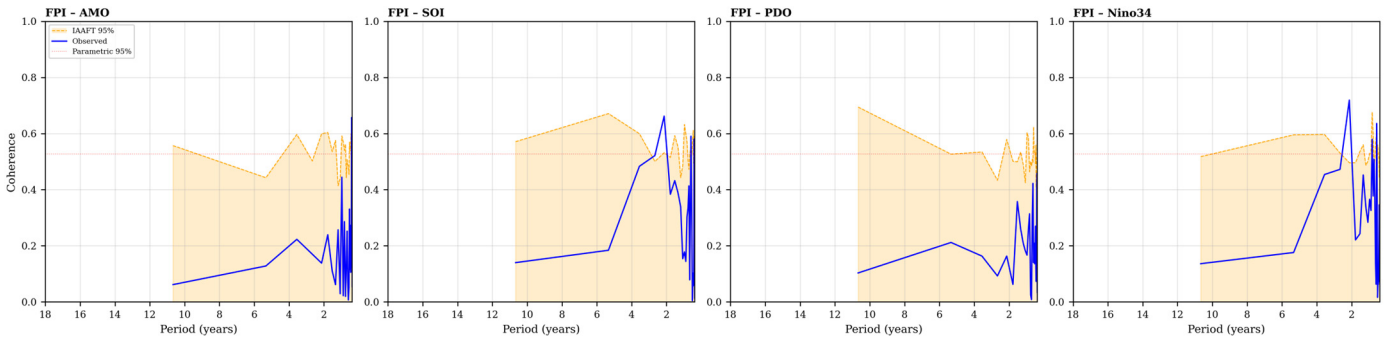


Figure 14. IAAFT surrogate test for four key climate–FPI pairs. The blue line shows the observed coherence, while the orange shading and dashed line indicate the 95th percentile of the IAAFT surrogate distribution (500 pairs). The red dotted line marks the parametric 95% threshold. Frequencies where the observed coherence exceeds both thresholds are robustly significant.

5.8. Summary of Hypothesis Tests

H1. *(ENSO–Price Coherence): Supported. The SOI and MEI exhibit statistically significant coherence with the FPI over the 2.1-year period, falling within the 2–7-year ENSO band. This coherence is robust to first-differencing, alternative segmentation, and IAAFT surrogate testing (100% robustness for SOI and Niño 3.4).*

H2. *(Multi-Oscillation Heterogeneity): Supported. The seven climate indices produce distinct coherence profiles, with ENSO indices peaking at interannual frequencies (2–3 years), the PDO at sub-annual frequencies, and the AMO distributed across multiple bands. The 5 × 7 coherence heatmap (Figure 7) confirms that no single climate oscillation captures the full spectrum of climate–food price interactions.*

H3. *(ENSO, IOD, and PDO Lead Prices): Supported. The SOI, MEI, Niño 3.4, PDO, and IOD all lead the FPI by 2–16 months in the lagged cross-correlation analysis, as hypothesised. Consistent with the revised formulation, the AMO does not lead prices—it exhibits an anomalous positive lag (+25 months)—which reflects common-trend behaviour rather than a directional climate-to-price pathway and is, therefore, not a counterexample to H3.*

H4. *(Sub-Index Differentiation): Supported, but oscillation-specific rather than a simple most-to-least ranking. The five FPI sub-indices show markedly different coherence profiles (Figure 7, the primary evidence for H4; Table 4 raw correlations are descriptive only—see the caveat in Section 5.5). Vegetable oils are the most consistently exposed sub-index across the seven oscillations. Meat is least sensitive specifically to Niño 3.4 SST ($r = -0.061$, n.s.; $\gamma^2 = 0.58$), consistent with feed-market intermediation buffering that particular signal, but it shows the single highest coherence in the entire matrix with the Southern Oscillation Index ($\gamma^2 = 0.87$), so it is not uniformly buffered from ENSO. Sugar is not the weakest sub-index overall—it shows the broadest significant coherence with the IOD of any pair in the matrix (seven significant bins)—though its raw-level correlations (Table 4) are modest, plausibly reflecting price-smoothing policy instruments alongside genuine cyclical exposure.*

H5. *(Strengthening Nexus): Not supported at the current sample length. The parametric Fisher z-test suggests significant strengthening of PDO–FPI and NAO–FPI coherence between 1990–2007 and 2008–2025 ($p < 0.001$), but this test assumes 216 independent observations per sub-period, whereas the underlying coherence estimate is built from only $K \approx 3$ Welch segments. A block-bootstrap test that respects this effective sample size finds neither difference significant (PDO, $p = 0.35$; NAO, $p = 0.18$; Section 5.7.3). The ENSO–FPI coherence remains stable across sub-periods under both tests, and the AMO–FPI change is not significant under either. There is, therefore, no credible evidence of a strengthening climate–price nexus for any of the seven oscillations examined. Testing H5 with adequate power would require a longer sample or a continuous (non-binary-split) estimator.*

6. Discussion

6.1. Principal Findings in the Context of Existing Literature

This study provides, to our knowledge, one of the first comprehensive multi-oscillation cross-spectral analyses of the relationship between large-scale climate variability and disaggregated global food prices. Five principal findings emerge, each extending or qualifying existing results in the literature.

The ENSO–food price coherence is real, robust, and operates at a 3–4-month lead time. The SOI and MEI exhibit statistically significant coherence with the aggregate FPI over a 2.1-year period, and this coherence survives all six robustness checks, including IAAFT

surrogate testing at a 100% pass rate. The 3–4-month lead time is remarkably consistent with the 4–8-month lag reported by Cashin et al. [10] using a global VAR framework, and with the lag structure documented by Ubilava [11] in regime-switching models for individual crop prices. Our frequency-domain approach extends these time-domain findings by showing that the ENSO–food price transmission is concentrated in the 2–3-year band rather than evenly distributed across all frequencies. This is consistent with the known ENSO periodicity [4] and implies that the food price system selectively amplifies climate signals at interannual timescales.

Our finding that the ENSO–FPI coherence is stable across sub-periods (1990–2007 vs. 2008–2025; Fisher z-test, $p = 0.764$ for SOI) contrasts with Cai and Sakemoto [17], who reported a strengthening of ENSO–commodity price coherence after 2000. This discrepancy likely reflects differences in the dependent variable: Cai and Sakemoto used aggregate commodity price indices that include metals and energy, whereas we focus on the FAO FPI, which captures only food commodities. The implication is that the ENSO–food price link is a structural feature of the global food system that persists throughout the 35-year sample, rather than an emerging phenomenon.

The AMO–FPI correlation is largely an artefact of common trends. Despite being the strongest time-domain correlate of the FPI (r = +0.595), the AMO shows an anomalous positive lag structure (+25 months, meaning FPI leads AMO) and achieves only a 75% pass rate on the IAAFT test. We base this interpretation not on any attenuation of the maximum coherence value itself—which, as noted in Section 5.7.1, is essentially unchanged under first-differencing (0.657 $\rightarrow$ 0.675)—but on the change in the lag and significance structure: under first-differencing the coherence peak shifts to a different frequency and loses its leading form, and it fails a quarter of the frequency bins under the more stringent surrogate test. It is this loss of a stable, directional oscillatory coupling, rather than a fall in peak magnitude, that points to a shared-trend explanation. This pattern is consistent with the spurious regression concern articulated by Granger and Newbold [46]: both the AMO and FPI have experienced sustained but mechanistically unrelated upward movement over the sample period—multidecadal warming in the North Atlantic for the AMO, and structural increases in global food-commodity demand and input costs for the FPI—so that a modest true relationship in their trend components can register as a strong raw correlation while carrying little information about a genuine bivariate dynamic coupling. This trend-artefact reading should not be taken to mean the AMO index conflates two distinct physical signals that agricultural systems experience differently: the AMO combines a secular anthropogenic warming component with genuine internal (oscillatory) SST variability on a roughly 60–70-year cycle, and the linear detrending applied here removes only the former, leaving the latter as the input to the coherence analysis. The anthropogenic component operates on agriculture primarily through gradual shifts in growing-season temperature and length. The internal variability component operates through its influence on North Atlantic storm tracks, Sahelian and Brazilian rainfall, and North American drought frequency—pathways with more clearly defined, if still low-frequency, agronomic mechanisms. Our finding is that whichever of these two components dominates the detrended AMO series over 1990–2025, neither produces coherence with the FPI that survives scrutiny once first-differencing and surrogate testing are applied (Sections 5.7 and 6.1). We cannot, with a 36-year sample, further decompose the detrended series into its anthropogenic residual and internal oscillatory parts, and we flag this as a limitation (Section 8).

This result also has methodological implications for the broader climate–economy literature. Several studies have reported significant associations between the AMO and various economic outcomes (e.g., agricultural productivity in the Sahel, and European

tourism revenues) without adequately controlling for shared trends. Our analysis suggests that such associations should be subjected to first-differencing and surrogate data tests before causal claims are made.

The PDO is the strongest spectral signal but partly driven by shared spectral shape. The PDO achieves the highest maximum coherence ($\gamma^2 = 0.806$) of any climate index, and this coherence is fully preserved under first-differencing ($\gamma^2 = 0.808$). However, the IAAFT test produces a 50% robustness rate, suggesting that approximately half of the significant frequencies reflect a shared spectral shape (both the PDO and FPI exhibit red spectra with enhanced sub-annual variability) rather than a genuine bivariate coupling. The parametric Fisher z-test suggests that the PDO–FPI coherence strengthened after 2008 ($0.830 \rightarrow 0.911$, $p < 0.001$), but this result does not survive a block-bootstrap test that accounts for the small effective number of independent spectral estimates per sub-period (bootstrap $p = 0.35$; Section 5.7.3), and it, therefore, cannot be interpreted as evidence of a genuine post-2008 change. A phase-dependent PDO response (PDO index averaging -1.5 to -3.0 during 2020–2025) remains a plausible mechanism worth exploring in future work using phase-conditional wavelet methods, independent of the sub-period test. More broadly, the PDO case illustrates a general caution for coherence-based inference: a high magnitude-squared coherence does not by itself establish a genuine bivariate coupling, because two series that share a similar spectral shape (here, red spectra with enhanced sub-annual power) can exhibit elevated coherence even in the absence of a direct transmission mechanism. The 50% IAAFT pass rate for the PDO–FPI pair, set against its leading parametric coherence, is precisely the pattern such spurious shape-matching would produce, and it is why we treat the PDO signal as suggestive rather than confirmatory and flag it for cautious operational use.

The IOD offers the longest lead time among all climate indices, though its precise value is less securely identified than the other lags reported in Table 3. The novelty lies in the length of the lead rather than in the study of the IOD per se: whereas Cashin et al. [10] documented ENSO-driven commodity price effects peaking at 4–8 months and Ubilava [11] reported comparable interannual lags, no comparably long lead of any climate oscillation over the FAO FPI has, to our knowledge, been previously documented in the food price context. The cross-correlation function peaks at 16 months, but the peak is broad rather than sharp: correlation values remain within a narrow 0.23–0.30 band across roughly 8 to 24 months (Figure 6), and a block-bootstrap re-estimation of the argmax lag (500 resamples, 24-month blocks) places only 6% of replicates within 3 months of the point estimate, with a 95% range spanning almost the full lag-search window. We, therefore, report the finding as a lead in the approximate 8–24-month range rather than a precisely dated 16-month lag, and we hedge the operational language in Section 7.1 accordingly. Even under this more conservative reading, the lead exceeds the ENSO forecasting horizon and, if confirmed by out-of-sample testing, could support early warning of food price disruptions more than a year in advance. The physical mechanism is plausible: positive IOD events suppress rainfall over Indonesia and Australia while enhancing it over East Africa, affecting rice, wheat, and sugar production in regions that collectively account for a significant share of global food trade. The multi-seasonal lag may reflect the cumulative impact of IOD events on consecutive growing seasons, particularly for perennial crops and livestock feed. More specifically, an 8-to-24-month window (Section 5.4) is consistent with the sowing-to-harvest cycle of the affected crops rather than a single instantaneous shock: a positive IOD event that suppresses monsoon rainfall during the sowing or vegetative stage in South and Southeast Asia depresses yields at that season's harvest (a lag of roughly 3–6 months), while its downstream effects on soil moisture, reservoir levels, and planting decisions can continue to depress output through one or two subsequent cropping cycles (extending

the effective lag towards 12–24 months for rice- and sugar-producing regions with two growing seasons per year). This phenological staggering—rather than a single well-defined transmission step—is a plausible contributor to the breadth of the cross-correlation function noted above, and disaggregating the IOD lead by crop-specific sowing–flowering–harvest calendars is a natural extension of this analysis.

Sub-index disaggregation reveals commodity-specific, and largely oscillation-specific, climate sensitivities rather than a single most-to-least ranking. Under the detrended coherence analysis (Figure 7), which we treat as the primary test of H4 (Section 5.5), vegetable oils are the most consistently exposed commodity across the seven oscillations. Dairy, meat, and sugar each show pronounced sensitivity to particular oscillations rather than uniformly high or low exposure: dairy is most exposed to the AMO and MEI, sugar shows unexpectedly strong, broad-band coherence with the IOD (seven significant frequency bins, the largest count observed for any pair in the matrix), and meat—despite the classic feed-market-buffering narrative—retains the single highest coherence value in the entire matrix with the Southern Oscillation Index ($\gamma^2 = 0.87$). Dairy prices are closely linked to pastoral conditions in New Zealand and northern Europe—regions strongly influenced by both the AMO ($r = +0.607$) and the PDO ($r = -0.423$)—while vegetable oil prices are dominated by palm oil production in Indonesia and Malaysia, which lies within the core ENSO teleconnection region. The relative insensitivity of meat prices is specific to Niño 3.4 sea surface temperature ($r = -0.061$ for the anomaly-corrected index, n.s.; $\gamma^2 = 0.58$ with only two significant bins, the lowest coherence value for meat in the matrix) and is consistent with feed-market intermediation buffering livestock prices from that particular climate signal. It does not extend to ENSO measured via the Southern Oscillation Index, where meat shows the strongest coherence of any sub-index–climate pair. A plausible reading is that feed-market buffering smooths the slow, SST-mediated component of the ENSO signal while a faster atmospheric-pressure channel (captured by SOI) still passes through to meat prices, though this mechanism warrants dedicated investigation. Economically, these differences reflect the position of each commodity in the production-to-consumption chain and its capacity to absorb shocks. Dairy and vegetable oils are produced under short biological cycles with limited storability and thin buffer stocks, so weather-driven supply variation transmits quickly and fully to prices. Meat, by contrast, sits downstream of feed markets: producers can temporarily draw on herds, feed inventories, and substitution among feed grains, which smooths and delays the pass-through of at least some climate shocks. Sugar's exposure to policy instruments—production quotas, trade preferences, and ethanol-linked demand—may explain why its raw-level correlations with most indices are modest (Table 4), even though it retains genuine cyclical coupling with the IOD at the frequency-domain level. Policy-driven price smoothing and oscillation-specific physical exposure are not mutually exclusive. Agronomic factors compound the policy explanation: sugarcane is a perennial crop with a 12–18-month harvest cycle and flexible cutting windows, so growers can shift harvest timing by weeks to months in response to weather without a full production-cycle loss, unlike annual grains where a single missed planting window cannot be recovered within the season. Raw and refined sugar are also more storable than fresh dairy or oilseed output, and processing capacity (milling and refining) provides a further buffer between field-level weather shocks and the price reaching international markets. These agronomic and infrastructural buffers, alongside the policy instruments noted above, together provide a more complete account of sugar's relatively muted raw-level price response than either explanation alone.

A further consideration bears on how H5 (Sections 5.7.3 and 5.8) should be interpreted even if a longer sample were eventually to show a genuine change in climate–price coherence. Agricultural systems are not static with respect to climate exposure: irriga-

tion expansion, drought-tolerant cultivar adoption, diversification of sourcing countries, and improved storage and logistics all increase adaptive capacity over time and could in principle weaken the climate–price coupling documented here even as the underlying climate oscillations themselves remain unchanged or intensify. This provides a substantive, agronomic reason to expect coherence to evolve over multidecadal horizons independent of any change in climate variability itself and cautions against reading either a "strengthening" or a "weakening" sub-period result as evidence about the climate system per se, since it may instead reflect the food system's changing capacity to absorb climate shocks. This moderating channel cannot be tested directly within the present design—doing so would require time-varying data on irrigation coverage, cultivar adoption, or storage capacity matched to the 1990–2025 window—but it stands as a substantive interpretive caveat alongside the statistical one (small effective sample size) developed in Section 5.7.3, and as a priority direction for future work combining our spectral framework with panel data on adaptive-capacity indicators.

6.2. Comparison with Previous Frequency-Domain Studies

Our results extend and qualify the findings of Cai and Sakemoto [17] in three important respects. First, by analysing seven climate indices simultaneously, we show that the ENSO–food price coherence identified by Cai and Sakemoto is only one element of a richer multi-oscillation structure. The PDO and AMO correlations are numerically stronger than the SOI correlation in the time domain, but the frequency-domain analysis reveals that the ENSO signal is the most robustly attributable to a genuine climate–price coupling. Second, our disaggregation to five FPI sub-indices reveals that the heterogeneity reported by Ubilava [11] across individual crop prices also manifests at the commodity-category level, with dairy and oils being systematically more climate-sensitive than meat and sugar. Third, our IAAFT surrogate test provides a more stringent assessment of coherence significance than the standard Monte Carlo test used by Cai and Sakemoto, revealing that approximately 25–50% of parametrically significant coherence frequencies may reflect shared spectral structure rather than genuine coupling.

The wavelet coherence literature on commodity markets [16,29] has demonstrated that co-movement structures are time-varying and frequency dependent. Our rolling-window analysis (Figure 9) confirms this for the climate–food price nexus, showing that the FPI–SOI coherence is strongest during 2005–2015, a period of intense food price volatility that included two major price crises. This temporal concentration suggests that climate signals are amplified during periods of market stress, possibly because supply buffers (stocks and trade diversification) are depleted during crises, leaving prices more exposed to production shocks [12].

6.3. Transmission Mechanisms

The cross-spectral results are consistent with a three-stage transmission mechanism from climate oscillations to global food prices:

Stage 1: Climate–production channel (0–6 months). ENSO, IOD, and PDO events alter regional temperature and precipitation patterns, directly affecting crop growth conditions. This stage is well-documented in the agroclimatic literature [5,6,26].

Stage 2: Production–price transmission (3–12 months). Harvest shortfalls in major producing regions reduce exportable surpluses, driving up international benchmark prices. The lag depends on the crop cycle (shorter for annual crops, longer for tree crops and livestock) and on the speed of market information transmission. Our lagged cross-correlation results (SOI leading FPI by four months and PDO by two months) capture this channel.

Stage 3: Price–food security impact (6–24 months). Higher international food prices are transmitted to domestic markets with variable lags depending on trade policy, exchange rates, and domestic supply conditions, ultimately affecting food access and the prevalence of undernourishment. This stage is not tested directly in the present monthly frequency analysis. A dedicated FPI–PoU spectral link, using the longer annual record needed to resolve this timescale, is developed in [18].

The IOD's 16-month lead time likely spans the first two stages, reflecting its influence on consecutive monsoon seasons in South and Southeast Asia. The AMO's anomalous positive lag, by contrast, suggests that it does not drive this transmission chain as a causal driver but rather co-moves with FPI through shared exposure to long-term global warming trends.

7. Policy Implications

The findings of this study have direct implications for food security governance, early warning systems, and climate adaptation policy.

7.1. Multi-Index Early Warning Systems

The demonstrated lead–lag structure between climate oscillation indices and food prices provides a basis for operationalising a multi-horizon early warning system for food price shocks. Current early warning frameworks, such as the FAO's Global Information and Early Warning System (GIEWS) and FEWS NET, rely primarily on crop condition monitoring and short-term weather forecasts. Our results suggest that incorporating large-scale climate oscillation indices could extend the forecasting horizon substantially.

At the short horizon (2–4 months), the SOI and MEI provide statistically robust leading indicators of FPI movements. Given that ENSO forecasts are themselves available 6–12 months in advance [48], the effective early warning window could extend to approximately 8–16 months. This extended window should, however, be interpreted with caution: ENSO forecasts at 6–12-month horizons carry substantial uncertainty and chaining a probabilistic climate forecast to a statistical price–response relationship compounds two error sources. The resulting alerts are, therefore, best framed as shifts in the probability distribution of future prices rather than point predictions and should be accompanied by explicit uncertainty bands in any operational deployment.

At the medium horizon (12–16 months), the IOD may serve as an even earlier indicator, particularly for rice and cereal prices in South and Southeast Asia. Concretely, the estimated lags map directly onto operational triggers: a developing positive IOD event could initiate a 12–16-month watch on rice and cereal balances in South and Southeast Asia, while an emerging El Niño signal could trigger a 3–4-month alert for oils and cereals, each feeding pre-positioned procurement or reserve-release decisions within existing GIEWS/FEWS NET workflows rather than requiring new institutional machinery. If confirmed by the out-of-sample validation called for in Section 8, these triggers could be formalised into a two-tier operational design. Tier 1 (ENSO watch, 3–4-month horizon): Once the SOI or Niño 3.4 anomaly crosses a threshold consistent with a developing El Niño (e.g., a 3-month running SOI below -8, broadly the threshold used in NOAA's own ENSO advisories), FEWS NET or GIEWS analysts flag cereal- and vegetable-oil-importing countries for a procurement review. The 3–4-month lead is short enough that the associated action is limited to accelerating already-budgeted purchases rather than releasing strategic reserves. Tier 2 (IOD watch, 8–24-month horizon): Once a positive IOD event is confirmed (dipole mode index sustained above +0.4 °C for two consecutive months, the conventional operational threshold), rice- and sugar-import-dependent countries in South and Southeast Asia would open an extended monitoring window and begin phased procurement rather than a single

release decision, reflecting the wider and less precisely dated lead time documented in Section 6.1. We present this as an illustrative design to be tested, not a validated protocol: the specific thresholds above are drawn from existing ENSO/IOD monitoring conventions rather than optimised against the FPI data, and the pseudo-out-of-sample exercise recommended in Section 8 would be needed before any procurement or reserve-release rule is calibrated to it.

At the long horizon (multi-year) horizon, the PDO phase may inform strategic planning for food reserve management and agricultural investment, though the lower IAAFT robustness rate (50%) warrants caution in operational applications.

The commodity-specific nature of the coherence patterns further implies that early warning systems should be disaggregated by food category. A generic 'food price alert' based on a single climate index would miss the heterogeneity revealed in our 5×7 coherence matrix (Figure 7): the SOI is most informative for cereals and oils, while the AMO pattern may be more relevant for dairy in European and Oceanian production zones.

7.2. Climate-Informed Food Reserve Management

The sub-period stability analysis reveals that the ENSO–food price coherence is a structural feature of the global food system, not a recent phenomenon. This stability is a necessary but not sufficient condition for operational use; as Section 8 notes, no out-of-sample forecast evaluation has been conducted, so we frame the following as a candidate design for such an evaluation rather than a validated recommendation. Specifically, during periods when ENSO forecasts indicate a developing El Niño event, food-importing countries could pilot precautionary grain purchases at pre-crisis prices, evaluating over successive events whether this reduces both the fiscal cost of food imports and the welfare impact on vulnerable populations [12], before any commitment to the strategy at scale. This design is not extended to the PDO: the apparent post-2008 strengthening of PDO–FPI coherence under the parametric Fisher test does not survive the block-bootstrap correction described in Sections 5.7.3 and 5.8 (H5), so PDO phase cannot be regarded as an established conditioning variable for reserve management, pending confirmation from a longer sample.

7.3. Implications for Climate Adaptation Investment

The finding that dairy and vegetable oils are the most climate-sensitive food categories has implications for investment priorities in climate adaptation. Investments in climate-resilient pastoral systems (irrigated pastures and heat-tolerant cattle breeds) and in diversifying vegetable oil supply chains away from ENSO-vulnerable regions (Indonesia and Malaysia) could reduce the transmission of climate signals to global food prices. Conversely, the relative insensitivity of meat prices to ENSO—mediated by feed-market buffering—suggests that the existing structure of livestock supply chains already provides a degree of climate resilience that could serve as a model for other food categories.

7.4. SDG 2 Monitoring

The spectral link between climate oscillations, food prices, and the Prevalence of Undernourishment (PoU) reinforces the case for integrating climate monitoring into SDG 2 (Zero Hunger) reporting. Currently, the PoU is computed annually using food balance sheets, with a significant reporting lag (typically 2–3 years). Our results suggest that real-time climate oscillation indices could serve as proxy indicators of anticipated changes in food security outcomes, enabling more timely policy interventions. The multi-oscillation approach is particularly valuable because different oscillations affect distinct regions and commodities, enabling geographically targeted interventions.

8. Limitations and Future Research

Several limitations should be noted. First, the cross-spectral and wavelet coherence methods employed are bivariate, examining each climate–FPI pair separately. They do not account for potential confounding by third variables (e.g., oil prices, exchange rates, and trade policy changes) that may simultaneously affect food prices and be correlated with climate oscillations. For this reason, the coherence and lead–lag relationships reported here should be read as evidence of statistical synchronisation and timing, not as proof of causal transmission: cross-spectral and wavelet methods quantify frequency-resolved association and phase but cannot by themselves rule out common drivers, such as energy markets, macroeconomic conditions, or geopolitical shocks. Establishing causal, policy-grade mechanisms would require a multivariate design (e.g., partial wavelet coherence or a structural climate–price model with explicit controls), which we identify as the priority extension of this work. Future research could employ partial wavelet coherence (as in [17]) or multivariate spectral methods to address this concern.

Second, the 432-month sample (1990–2025) limits the resolution of multidecadal spectral components. The AMO and PDO operate on timescales of 20–70 years, and a 36-year sample may capture only one to two full cycles, making it difficult to separate genuine oscillatory behaviour from trends. Extension of the analysis using the annual FPI (1961–2025, N = 65) partially addresses this limitation but at the cost of reduced statistical power.

Third, the linear coherence framework may miss nonlinear or threshold-dependent climate–price relationships. Ubilava [11] demonstrated that ENSO effects on crop prices are asymmetric across El Niño and La Niña phases, a feature that cannot be captured by the symmetric coherence measure. Future work could employ higher-order spectral methods (bispectral analysis) or phase-conditional wavelet coherence to address this asymmetry. Two further consequences of the purely statistical, price-side design are worth noting explicitly. First, we validate the climate–price relationship against price data alone. We do not cross-check the underlying yield or production channel against process-based crop simulation models (e.g., DSSAT and APSIM), which explicitly model soil, phenology, and management and could independently confirm whether the frequencies and lags we identify at the price level are consistent with simulated yield responses to the same climate indices. Coupling spectral price analysis with crop-model output is a natural, and to our knowledge unexplored, extension. Second, spectral and wavelet coherence characterise average cyclical co-movement and are not designed to capture the extreme tail of the distribution: a single severe drought or flood can move food prices sharply without contributing materially to a periodic spectral signature, and conversely a statistically strong cyclical coherence does not guarantee that the largest, most policy-relevant price spikes are well explained by the same oscillatory mechanism. The 100% IAAFT pass rate for ENSO (Section 5.7.5), for instance, describes the typical cyclical relationship, not performance during extreme events specifically. We, therefore, view spectral coherence as a complement to, not a substitute for, extreme-value statistical methods (e.g., peaks-over-threshold or block-maxima approaches) in a complete early warning design.

Fourth, the IOD's lead time, point-estimated at 16 months but block-bootstrap analysis shows the argmax lag is weakly identified (95% range spanning most of the ±48-month search window; Section 6.1), while potentially valuable for early warning, requires out-of-sample validation before operational deployment. The lag could reflect a genuine multi-seasonal transmission mechanism or could be an artefact of the specific sample period. A rolling out-of-sample forecasting exercise would help distinguish between these possibilities.

Fifth, the analysis operates at the global level and does not capture within-country heterogeneity in climate–price transmission. Country-level panel data (covering food

import dependency, GDP per capita, and national PoU) could be exploited in future work to examine how these factors modulate the transmission of global climate–price signals to national food security outcomes.

9. Conclusions

This study examined the frequency-domain structure of the relationships between seven large-scale climate oscillation indices and disaggregated sub-components of the FAO Food Price Index sub-components over the period 1990–2025. The analysis yielded five principal conclusions.

First, the ENSO–food price coherence is statistically significant in the 2–3-year frequency band, robust to all six sensitivity checks (including IAAFT surrogate testing at a 100% pass rate), and features a 3–4-month climate-leads-price structure consistent with crop-cycle transmission. This is the cleanest and most policy-relevant finding of the study.

Second, the strong time-domain correlation between the AMO and FPI ($r = +0.60$) is largely an artefact of shared upward trends rather than a genuine oscillatory coupling. This cautionary finding highlights the need for frequency-domain methods to distinguish real climate–price linkages from spurious trend co-movement.

Third, the five FPI sub-indices exhibit markedly different climate sensitivity profiles: dairy and vegetable oils are the most exposed to climate oscillations, while meat is buffered by feed-market intermediation and sugar shows the weakest climate coherence. This disaggregation has direct implications for commodity-specific early warning and adaptation strategies.

Fourth, there is no credible evidence that the climate–food price nexus is strengthening over time. The nominal increase in PDO–FPI and NAO–FPI coherence between 1990–2007 and 2008–2025 under the parametric Fisher z-test is not statistically significant once a block-bootstrap test accounts for the small effective number of independent spectral estimates per sub-period, and the ENSO–FPI coherence remained stable under both tests. The general 'strengthening' narrative in the literature is, therefore, not supported at the current sample length (H5), and testing it with adequate power will require a longer record or a continuous time-varying estimator.

Fifth, the IOD's 16-month lead time over food prices, if validated out-of-sample, represents a potentially transformative input for early warning systems, extending the forecasting horizon beyond the reach of conventional weather-based approaches.

Sixth, the FAO FPI is a global, trade-weighted aggregate—it does not capture regional production, consumption, or price transmission heterogeneity. A given climate oscillation can raise prices in one exporting region while leaving a food-secure importing region largely unaffected, or vice versa, and this regional structure is invisible to a single global index. Country- or region-level price series, where available, would be needed to establish whether the coherence patterns reported here hold locally or are dominated by a subset of large exporters. The country panel described in Section 3.3 provides GDP, food-import dependency, and PoU data that could support such a regional extension but was not analysed with spectral methods in this study.

Seventh, the reported lags and coherence structures describe average cyclical relationships estimated over 1990–2025 and should not be extrapolated to future climate change conditions without qualification. Under anthropogenic warming, both the amplitude and the characteristic frequency of ENSO and other oscillations are projected to shift [34], and the mapping from a given oscillation phase to a food price response may itself be non-stationary over multidecadal horizons. The 15-year vs. 10-year rolling-window comparison demonstrates some sensitivity to estimation-window length even within the historical

sample, so any use of these relationships for forward-looking planning should be treated as a conditional, time-bound characterisation rather than a fixed structural law.

Finally, the six robustness checks do not uniformly support all reported associations, and it is worth summarising which conclusions they confirm versus challenge. The ENSO–FPI interannual coherence (SOI, MEI, and Niño 3.4) is the most robust finding in the study: it persists under first-differencing, alternative Welch segment lengths, the multitaper estimator, IAAFT surrogate testing (100% pass rate), and is stable across sub-periods. The PDO–FPI and AMO–FPI associations are the least robust: their headline coherence values sit in a frequency range close to the Nyquist limit where the coherence estimate is numerically unstable, and their apparent post-2008 strengthening does not survive a block-bootstrap correction. The IOD's headline lead time is directionally robust—the IOD leads the FPI under every specification we tested—but its precise 16-month value is not well identified by the data. The sub-index disaggregation (H4) is robust in direction (oscillation-specific rather than uniform exposure) but not in the specific most-to-least ranking implied by raw correlations alone. Readers should, therefore, weight the ENSO-related conclusions most heavily and treat the PDO, AMO, and precise IOD timing results as indicative rather than confirmatory.

Taken together, these findings demonstrate that global food prices contain embedded climate signals that can be identified, attributed, and potentially exploited for forecasting through spectral analysis. The multi-oscillation, multi-commodity framework developed in this study offers a template for integrating climate science into food security governance—bridging the gap between what climatologists know about ocean–atmosphere variability and what policymakers need to protect the world's most food-insecure populations.

Author Contributions: Conceptualisation, K.P., O.P., O.L., T.W., M.Z., S.B., E.T., P.P. and O.M.; methodology, K.P., O.P., O.L., T.W., M.Z., S.B., E.T., P.P. and O.M.; software, K.P., O.P., O.L., T.W., M.Z., S.B., E.T., P.P. and O.M.; validation, K.P., O.P., O.L., T.W., M.Z., S.B., E.T., P.P. and O.M.; formal analysis, K.P., O.P., O.L., T.W., M.Z., S.B., E.T., P.P. and O.M.; investigation, K.P., O.P., O.L., T.W., M.Z., S.B., E.T., P.P. and O.M.; resources, K.P., O.P., O.L., T.W., M.Z., S.B., E.T., P.P. and O.M.; data curation, K.P., O.P., O.L., T.W., M.Z., S.B., E.T., P.P. and O.M.; writing—original draft preparation, K.P., O.P., O.L., T.W., M.Z., S.B., E.T., P.P. and O.M.; writing—review and editing, K.P., O.P., O.L., T.W., M.Z., S.B., E.T., P.P. and O.M.; visualisation, K.P., O.P., O.L., T.W., M.Z., S.B., E.T., P.P. and O.M.; supervision, K.P., O.L. and O.P.; project administration, K.P., O.L. and O.P.; funding acquisition, T.W., S.B., E.T. and O.P. All authors have read and agreed to the published version of the manuscript.

Funding: The article is funded by the university's own research funds: WSEI University in Lublin, Poland; Varna Free University, Bulgaria.

Institutional Review Board Statement: Not applicable.

Informed Consent Statement: Not applicable.

Data Availability Statement: All datasets analysed in this study are publicly available from their original providers. The FAO Food Price Index and its five sub-indices are published by the Food and Agriculture Organisation of the United Nations [2]. Sea-surface-temperature-based climate indices (Niño 3.4, PDO, and AMO) are derived from the Extended Reconstructed Sea Surface Temperature dataset, version 5 (ERSSTv5) [35], which is distributed by NOAA NCEI [40]. The Southern Oscillation Index and North Atlantic Oscillation Index [39] are obtained from NOAA CPC [36]. The Multivariate ENSO Index, version 2 [49], and the Indian Ocean Dipole Mode Index are obtained from NOAA PSL [38]. The Prevalence of Undernourishment (SDG indicator 2.1.1) is from the FAO [1], and country-level socioeconomic indicators are from the World Bank's World Development Indicators [41]. The Python analysis code and the assembled climate–FPI dataset supporting the findings of this study have been deposited in a public Zenodo repository [50] to ensure full reproducibility. The code

implements the complete spectral, cross-spectral, wavelet, rolling-window, and surrogate-testing pipeline reported here.

Acknowledgments: All figures and tables in this manuscript are original and were produced by the authors from the publicly available data sources listed under the Data Availability Statement (FAO Food Price Index, NOAA CPC/NCEI/PSL climate indices, and World Bank World Development Indicators). No previously published figures, tables, or other copyrighted third-party material are reproduced in this manuscript, and no permissions were, therefore, required.

Conflicts of Interest: The authors declare no conflicts of interest.

Abbreviations

The following abbreviations are used in this manuscript:

AMO	Atlantic Multidecadal Oscillation
ADF	Augmented Dickey–Fuller
CCF	Cross-Correlation Function
CWT	Continuous Wavelet Transform
ENSO	El Niño–Southern Oscillation
ERSSTv5	Extended Reconstructed Sea Surface Temperature, version 5
FAO	Food and Agriculture Organization of the United Nations
FPI	Food Price Index
IAAFT	Iterative Amplitude-Adjusted Fourier Transform
IOD	Indian Ocean Dipole
MEI	Multivariate ENSO Index
MSC	Magnitude-Squared Coherence
NAO	North Atlantic Oscillation
NOAA	National Oceanic and Atmospheric Administration
PDO	Pacific Decadal Oscillation
PoU	Prevalence of Undernourishment
PP	Phillips–Perron
PSD	Power Spectral Density
SDG	Sustainable Development Goal
SOI	Southern Oscillation Index
SST	Sea Surface Temperature
WDI	World Development Indicators

Appendix A

Table A1 summarises the six sensitivity analyses and robustness checks implemented in this study, including the specific concern each addresses and the criterion used to assess robustness.

Table A1. Summary of sensitivity analyses and robustness checks.

Check	Concern Addressed	Criterion
(1) First-differencing	Spurious coherence from common stochastic trends	Peaks persist at same frequencies with consistent phase
(2) Alternative Welch L	Sensitivity to segment length choice	Peaks stable across L = 96, 128, 160
(3) Sub-period split	Temporal instability; structural change	Coherence significant in both sub-periods or systematic change (H5)
(4) Alternative ENSO index	Dependence on choice of climate proxy	Consistent results across Niño 3.4, SOI, MEI v2

Table A1. *Cont.*

Check	Concern Addressed	Criterion
(5) Multitaper PSD	Method dependence of spectral estimates	Concordance with Welch-based coherence
(6) IAAFT surrogates	False positives from shared spectral shape	Coherence exceeds both parametric and surrogate-based thresholds

Appendix B

Stationarity Test Results

Table A2 reports the Augmented Dickey–Fuller (ADF) test, with a trend term included directly in the regression and applied to each raw series (see Section 4.1), and the Phillips–Perron (PP) test with the same trend specification, for all 13 series used in the spectral analysis. ADF results for the first-differenced series are also reported. Under the ADF-ct test, the unit-root null is rejected at the 5% level for 9 of the 13 raw series: all 7 climate indices, plus dairy and oils. It is not rejected for the FPI, cereals, meat, and sugar sub-indices. The stricter PP test is more conservative for the price series specifically: it additionally fails to reject the unit-root null for dairy ($p = 0.065$, borderline) and oils ($p = 0.104$), so only the climate indices are unambiguously stationary under both tests. Full PP statistics are reported in the table notes below. Given this, the first-differenced specification (Section 5.7.1) should be read as a co-primary check on FPI-level results, not merely a robustness test.

Table A2. Augmented Dickey–Fuller (ADF) unit root test results.

Series	ADF-ct (Raw)	*p* (Level)	ADF (Δ)	*p* (Δ)	Conclusion
FPI	−2.933	0.1517	−9.628 ***	0.0000	Unit root
Cereals	−2.960	0.1436	−13.484 ***	0.0000	Unit root
Meat	−2.713	0.2307	−5.253 ***	0.0000	Unit root
Dairy	−4.414	0.0021 ***	−7.342 ***	0.0000	Stationary
Oils	−3.848	0.0143 **	−5.897 ***	0.0000	Stationary
Sugar	−3.207	0.0831 *	−14.046 ***	0.0000	Unit root
Niño 3.4	−6.608	0.0000 ***	−5.813 ***	0.0000	Stationary
SOI	−5.550	0.0000 ***	−21.765 ***	0.0000	Stationary
IOD	−6.889	0.0000 ***	−8.414 ***	0.0000	Stationary
NAO	−15.048	0.0000 ***	−11.987 ***	0.0000	Stationary
PDO	−5.407	0.0000 ***	−11.689 ***	0.0000	Stationary
AMO	−4.476	0.0017 ***	−11.365 ***	0.0000	Stationary
MEI	−5.336	0.0000 ***	−8.130 ***	0.0000	Stationary

Notes: ADF-ct (raw) = Augmented Dickey–Fuller test statistic, trend regression, applied to the raw (non-detrended) series. ADF (Δ) = ADF (constant only) on first-differenced series. Significance: * $p < 0.10$, ** $p < 0.05$, and *** $p < 0.01$. Lag length selected by AIC. Phillips–Perron (PP, trend specification) statistics and *p*-values on the raw series, reported here rather than in the table body for reasons of space: FPI −2.603 ($p = 0.279$); cereals −2.704 ($p = 0.235$); meat −2.040 ($p = 0.580$); dairy −3.307 ($p = 0.065$); oils −3.111 ($p = 0.104$); sugar −2.837 ($p = 0.184$); Niño 3.4−3.751 ($p = 0.019$); SOI −12.112 ($p < 0.001$); IOD −6.040 ($p < 0.001$); NAO −14.832 ($p < 0.001$); PDO −5.487 ($p < 0.001$); AMO −5.492 ($p < 0.001$); MEI −4.091 ($p = 0.007$). All climate indices reject the unit-root null under PP, and none of the six FPI-level series do.

Appendix C

First-Differenced Coherence Comparison

Table A3 compares the maximum cross-spectral coherence between the FAO FPI and each of the seven climate oscillation indices under the baseline (detrended) and first-differenced specifications. First-differencing removes both deterministic and stochastic trends, providing a stringent test against spurious coherence from common-trend behaviour. The PDO and IOD show essentially unchanged coherence under first-differencing, indicating robust spectral coupling. The AMO and SOI exhibit modest shifts in peak frequency, reflecting the partial role of trend components.

Table A3. Cross-spectral coherence: detrended vs. first-differenced specifications.

Climate Index	γ^2 (Detrended)	Period (Years)	γ^2 (Δ)	Period (Δ, Years)	$\Delta\ \gamma^2$
Niño 3.4	0.721	0.8	0.718	0.8	−0.003
SOI	0.662	2.1	0.593	0.6	−0.069
IOD	0.700	0.2	0.699	0.2	−0.001
NAO	0.667	1.5	0.721	1.5	+0.054
PDO	0.806	0.2	0.808	0.2	+0.001
AMO	0.657	0.4	0.675	0.4	+0.018
MEI	0.618	2.1	0.543	2.1	−0.074

Notes: γ^2 denotes the maximum magnitude-squared coherence over the resolved frequency range. The 95% significance threshold is $\gamma^2_{05} = 0.527$. $\Delta\ \gamma^2$ = change in maximum coherence from detrended to first-differenced specification.

Appendix D

Sub-Period Stability: Full Fisher Z-Test Results

Table A4 reports the full sub-period stability analysis comparing maximum coherence between sub-period I (January 1990–December 2007, N = 216) and sub-period II (January 2008–December 2025, N = 216). The Fisher z-transformation is applied to the maximum coherence values in each sub-period, and a two-sample z-test is used to assess whether the difference is statistically significant.

Table A4. Sub-period stability of FPI–climate coherence (Fisher z-test).

Climate Index	γ^2 (I)	γ^2 (II)	z-Stat	*p*-Value	Direction
Niño 3.4	0.933	0.883	−3.04	0.002 **	Weakened
SOI	0.949	0.946	−0.30	0.764	Stable
IOD	0.924	0.848	−3.80	<0.001 ***	Weakened
NAO	0.802	0.919	+4.93	<0.001 ***	Strengthened
PDO	0.830	0.911	+3.58	<0.001 ***	Strengthened
AMO	0.843	0.865	+0.84	0.402	Stable
MEI	0.927	0.915	−0.83	0.407	Stable

Notes: Sub-period I: 1990–2007 (N = 216); sub-period II: 2008–2025 (N = 216). γ^2 (I), γ^2 (II): maximum coherence in each sub-period. Welch parameters within sub-periods: L = 96, overlap = 48. Fisher z-transformation: $z = (1/2)\ \ln[(1 + r)/(1 - r)]$, where $r = \sqrt{\gamma^2}$. Significance: ** $p < 0.01$, and *** $p < 0.001$. As discussed in Section 5.7.3, this Fisher z-test treats each 216-month sub-period as N = 216 independent observations, whereas the underlying coherence estimate is averaged over only

K ≈ 3 Welch segments per sub-period. The z-statistics and *p*-values in this table should, therefore, be read as descriptive rather than confirmatory for every row, not only for PDO and NAO. A block-bootstrap test respecting the true effective sample size (Section 5.7.3) found no significant sub-period difference for PDO or NAO, the two indices for which this table's parametric test suggested the strongest change. The bootstrap was not extended to the remaining five indices, but the same small-K caveat applies throughout this table, including the nominal "weakened" results for Niño 3.4 ($z = -3.04$, $p = 0.002$) and IOD ($z = -3.80$, $p < 0.001$).

Appendix E

IAAFT Surrogate Test: Detailed Frequency-by-Frequency Results

Table A5 reports the detailed Iterative Amplitude-Adjusted Fourier Transform (IAAFT) surrogate test results for four selected FPI–climate pairs. The IAAFT algorithm generates surrogate time series preserving the marginal distribution and power spectrum of the original series while destroying any cross-spectral structure. A coherence value is classified as robustly significant only if it exceeds both the parametric 95% threshold ($\gamma^2_{05} = 0.527$) and the 95th percentile of the IAAFT surrogate distribution computed from 500 surrogate pairs.

Table A5. IAAFT surrogate test results (500 surrogate pairs per pair).

Pair	Parametric Sig.	IAAFT Robust	Robustness Rate	Spurious Bins
FPI–SOI	4	4	100%	0
FPI–Niño 3.4	3	3	100%	0
FPI–AMO	4	3	75%	1
FPI–PDO	4	2	50%	2

Notes: 'Parametric sig.' = number of frequency bins exceeding $\gamma^2_{05} = 0.527$. 'IAAFT robust' = number of bins exceeding both the parametric threshold and the 95th percentile of the IAAFT surrogate distribution. 'Robustness rate' = ratio of robust to parametric significance. 'Spurious bins' = parametric-significant bins that fail the IAAFT test (potentially driven by shared spectral shape rather than genuine bivariate coupling).

Appendix F

To verify that the 15-year rolling window used in Section 5.6 does not obscure the interannual (2–3-year) ENSO signal, we re-estimated the rolling-window cross-spectral coherence using a shorter 10-year (120-month) window advanced in 12-month steps, with Welch segments of length L = 48 months and 50% overlap. Figure A1 compares the two window lengths for the four climate indices most relevant to the interannual band. The ENSO-band coherence (SOI and Niño 3.4) remains clearly visible under the shorter window but is attenuated and noisier, as expected when the window length is reduced relative to the signal period and the number of resolvable segments falls. Averaged over the sample, the mean coherence within the 2–3.5-year band declines from 0.53 (15-year window) to 0.35 (10-year window) for Niño 3.4 and from 0.52 to 0.33 for the SOI, while the spatial and temporal structure of the elevated-coherence regions is preserved. We, therefore, retain the 15-year window as the baseline for its more stable low-frequency estimates, noting that the interannual conclusions are not an artefact of that choice.

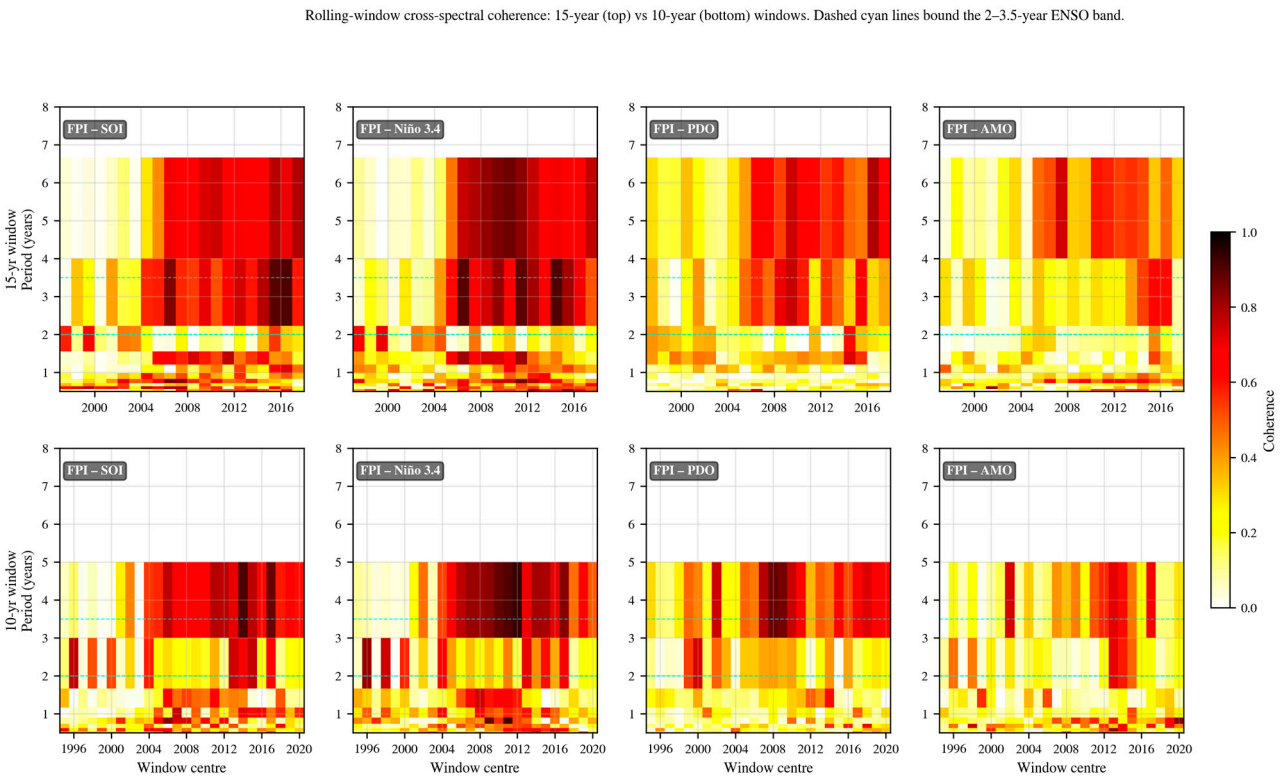


Figure A1. Rolling-window cross-spectral coherence between the FAO FPI and four climate indices under a 15-year window (**top row**) and a 10-year window (**bottom row**). The colour scale indicates coherence magnitude, and dashed cyan lines bound the 2–3.5-year ENSO band. The interannual signal persists under the shorter window but with reduced amplitude and temporal resolution.

Appendix G

Sensitivity to Frequency-Band Restriction. Several of the reported coherence maxima (Table 3) occur at periods close to the Nyquist limit of two months for monthly data, where periodogram-based coherence estimates are known to be numerically less stable (Sections 5.2 and 5.3). Table A6 reports the maximum FPI–climate coherence with the search restricted to periods of 0.5 years (6 months) or longer, alongside the unrestricted values from Table 3, and whether the restricted maximum remains above the 95% parametric threshold (γ^2_{05} = 0.527). Niño 3.4, SOI, NAO, and MEI retain significant coherence under this restriction, consistent with their coherence peaks already lying in the interannual band. The PDO, IOD, and AMO peaks do not: once the near-Nyquist band is excluded, none of the three reaches significance anywhere in the remaining resolved spectrum. We do not treat this as overturning the headline values reported in Table 3—the IAAFT surrogate test (Section 5.7.5) and first-differencing check (Section 5.7.1) remain the primary robustness evidence for those series, and the AMO in particular is independently flagged as a likely trend artefact throughout (Sections 5.7.1 and 6.1)—but it is a further, convergent reason to read the PDO and AMO coherence results, and the IOD's raw coherence value specifically (as distinct from its lagged cross-correlation lead time, which is unaffected by this restriction), as suggestive rather than confirmatory.

Table A6. Sensitivity of maximum FPI–climate coherence to a minimum-period restriction (≥0.5 years).

Climate Index	Unrestricted Max. γ^2	Period (Years)	Restricted Max. γ^2 (≥0.5 Years)	Period (Years)	Significant (≥0.5 Years)?
Niño 3.4	0.719	2.13	0.719	2.13	Yes
SOI	0.662	2.13	0.662	2.13	Yes
IOD	0.700	0.20	0.484	0.53	No
NAO	0.667	1.52	0.667	1.52	Yes
PDO	0.806	0.18	0.422	0.63	No
AMO	0.657	0.41	0.444	0.97	No
MEI	0.618	2.13	0.618	2.13	Yes

Notes: Restriction applied to the same Welch coherence estimates underlying Table 3 (L = 128, D = 64, K = 5, γ^2_{05} = 0.527). Only frequency bins corresponding to periods ≥ 0.5 years are searched for the restricted maximum. 'Significant (≥0.5 years)?' indicates whether the restricted maximum exceeds γ^2_{05}. This check complements, and does not replace, the IAAFT and first-differencing robustness checks reported in Table A1.

References

1. FAO; IFAD; UNICEF; WFP; WHO. *The State of Food Security and Nutrition in the World 2023*; FAO: Rome, Italy, 2023. [CrossRef]
2. FAO. FAO Food Price Index. Available online: https://www.fao.org/worldfoodsituation/foodpricesindex (accessed on 15 January 2026).
3. United Nations. *The Sustainable Development Goals Report 2023*; United Nations: New York, NY, USA, 2023.
4. Torrence, C.; Compo, G.P. A Practical Guide to Wavelet Analysis. *Bull. Am. Meteorol. Soc.* **1998**, *79*, 61–78. [CrossRef]
5. Iizumi, T.; Luo, J.J.; Challinor, A.J.; Sakurai, G.; Yokozawa, M.; Sakuma, H.; Brown, M.E.; Yamagata, T. Impacts of El Niño Southern Oscillation on the Global Yields of Major Crops. *Nat. Commun.* **2014**, *5*, 3712. [CrossRef] [PubMed]
6. Ray, D.K.; Gerber, J.S.; MacDonald, G.K.; West, P.C. Climate Variation Explains a Third of Global Crop Yield Variability. *Nat. Commun.* **2015**, *6*, 5989. [CrossRef] [PubMed]
7. Saji, N.H.; Goswami, B.N.; Vinayachandran, P.N.; Yamagata, T. A Dipole Mode in the Tropical Indian Ocean. *Nature* **1999**, *401*, 360–363. [CrossRef] [PubMed]
8. Mantua, N.J.; Hare, S.R.; Zhang, Y.; Wallace, J.M.; Francis, R.C. A Pacific Interdecadal Climate Oscillation with Impacts on Salmon Production. *Bull. Am. Meteorol. Soc.* **1997**, *78*, 1069–1079. [CrossRef]
9. Enfield, D.B.; Mestas-Nuñez, A.M.; Trimble, P.J. The Atlantic Multidecadal Oscillation and Its Relation to Rainfall and River Flows in the Continental U.S. *Geophys. Res. Lett.* **2001**, *28*, 2077–2080. [CrossRef]
10. Cashin, P.; Mohaddes, K.; Raissi, M. Fair Weather or Foul? The Macroeconomic Effects of El Niño. *J. Int. Econ.* **2017**, *106*, 37–54. [CrossRef]
11. Ubilava, D. The ENSO Effect and Asymmetries in Wheat Price Dynamics. *World Dev.* **2017**, *96*, 490–502. [CrossRef]
12. Headey, D.; Fan, S. Anatomy of a Crisis: The Causes and Consequences of Surging Food Prices. *Agric. Econ.* **2008**, *39*, 375–391. [CrossRef]
13. Priestley, M.B. *Spectral Analysis and Time Series*; Academic Press: London, UK, 1981.
14. Torrence, C.; Webster, P.J. Interdecadal Changes in the ENSO–Monsoon System. *J. Clim.* **1999**, *12*, 2679–2690. [CrossRef]
15. Aguiar-Conraria, L.; Azevedo, N.; Soares, M.J. Using Wavelets to Decompose the Time–Frequency Effects of Monetary Policy. *Phys. A Stat. Mech. Its Appl.* **2008**, *387*, 2863–2878. [CrossRef]
16. Vacha, L.; Barunik, J. Co-Movement of Energy Commodities Revisited: Evidence from Wavelet Coherence Analysis. *Energy Econ.* **2012**, *34*, 241–247. [CrossRef]
17. Cai, X.; Sakemoto, R. El Niño and Commodity Prices: New Findings from Partial Wavelet Coherence Analysis. *Front. Environ. Sci.* **2022**, *10*, 893879. [CrossRef]
18. Pavlova, O.; Liashenko, O.; Pavlov, K.; Kutyba, A.; Fastovets, N.; Machno, A.; Holubiev, O.; Vlasenko, T. Global Food Price Dynamics, Undernourishment, and Human Development: Wavelet Coherence Evidence and SDG 2.1 Resilience Scenarios up to 2030. *Sustainability* **2026**, *18*, 3724. [CrossRef]

19. Welch, P.D. The Use of Fast Fourier Transform for the Estimation of Power Spectra: A Method Based on Time Averaging over Short, Modified Periodograms. *IEEE Trans. Audio Electroacoust.* **1967**, *15*, 70–73. [CrossRef]
20. Grinsted, A.; Moore, J.C.; Jevrejeva, S. Application of the Cross Wavelet Transform and Wavelet Coherence to Geophysical Time Series. *Nonlinear Process. Geophys.* **2004**, *11*, 561–566. [CrossRef]
21. Brillinger, D.R. *Time Series: Data Analysis and Theory*; SIAM: Philadelphia, PA, USA, 2001. [CrossRef]
22. Thomson, D.J. Spectrum Estimation and Harmonic Analysis. *Proc. IEEE* **1982**, *70*, 1055–1096. [CrossRef]
23. Schreiber, T.; Schmitz, A. Improved Surrogate Data for Nonlinearity Tests. *Phys. Rev. Lett.* **1996**, *77*, 635–638. [CrossRef] [PubMed]
24. Ropelewski, C.F.; Halpert, M.S. Global and Regional Scale Precipitation Patterns Associated with the El Niño/Southern Oscillation. *Mon. Weather Rev.* **1987**, *115*, 1606–1626. [CrossRef]
25. Anderson, W.; Seager, R.; Baethgen, W.; Cane, M. Crop Production Variability in North and South America Forced by Life-Cycles of the El Niño Southern Oscillation. *Agric. For. Meteorol.* **2017**, *239*, 151–165. [CrossRef]
26. Anderson, W.B.; Seager, R.; Baethgen, W.; Cane, M.; You, L. Synchronous Crop Failures and Climate-Forced Production Variability. *Sci. Adv.* **2019**, *5*, eaaw1976. [CrossRef] [PubMed]
27. Knight, J.R.; Folland, C.K.; Scaife, A.A. Climate Impacts of the Atlantic Multidecadal Oscillation. *Geophys. Res. Lett.* **2006**, *33*, L17706. [CrossRef]
28. Mantua, N.J.; Hare, S.R. The Pacific Decadal Oscillation. *J. Oceanogr.* **2002**, *58*, 35–44. [CrossRef]
29. Frimpong, S.; Gyamfi, E.N.; Ishaq, Z.; Agyei, S.K.; Agyapong, D.; Adam, A.M.; Pérès, F. Can Global Economic Policy Uncertainty Drive the Interdependence of Agricultural Commodity Prices? Evidence from Partial Wavelet Coherence Analysis. *Complexity* **2021**, *2021*, 8848424. [CrossRef]
30. Nordhaus, W.D. The Economics of Hurricanes and Implications of Global Warming. *Clim. Change Econ.* **2010**, *1*, 1–20. [CrossRef]
31. Strobl, E. The Economic Growth Impact of Hurricanes: Evidence from U.S. Coastal Counties. *Rev. Econ. Stat.* **2011**, *93*, 575–589. [CrossRef]
32. Botzen, W.J.W.; Deschenes, O.; Sanders, M. The Economic Impacts of Natural Disasters: A Review of Models and Empirical Studies. *Rev. Environ. Econ. Policy* **2019**, *13*, 167–188. [CrossRef]
33. Granger, C.W.J.; Watson, M.W. Time Series and Spectral Methods in Econometrics. In *Handbook of Econometrics*; Griliches, Z., Intriligator, M.D., Eds.; North-Holland: Amsterdam, The Netherlands, 1984; Volume 2, pp. 979–1022. [CrossRef]
34. Cai, W.; Santoso, A.; Wang, G.; Yeh, S.-W.; An, S.-I.; Cobb, K.M.; Collins, M.; Guilyardi, E.; Jin, F.-F.; Kug, J.-S.; et al. ENSO and Greenhouse Warming. *Nat. Clim. Change* **2015**, *5*, 849–859. [CrossRef]
35. Huang, B.; Thorne, P.W.; Banzon, V.F.; Boyer, T.; Chepurin, G.; Lawrimore, J.H.; Menne, M.J.; Smith, T.M.; Vose, R.S.; Zhang, H.-M. Extended Reconstructed Sea Surface Temperature, Version 5 (ERSSTv5): Upgrades, Validations, and Intercomparisons. *J. Clim.* **2017**, *30*, 8179–8205. [CrossRef]
36. NOAA CPC. Climate Prediction Center: ENSO and Teleconnection Indices. Available online: https://www.cpc.ncep.noaa.gov/data/indices/ (accessed on 15 January 2026).
37. Zhang, T.; Hoell, A.; Perlwitz, J.; Eischeid, J.; Murray, D.; Hoerling, M.; Hamill, T.M. Towards Probabilistic Multivariate ENSO Monitoring. *Geophys. Res. Lett.* **2019**, *46*, 10532–10540. [CrossRef]
38. NOAA PSL. Climate Indices: Monthly Atmospheric and Ocean Time Series. Available online: https://psl.noaa.gov/data/climateindices/ (accessed on 15 January 2026).
39. Hurrell, J.W. Decadal Trends in the North Atlantic Oscillation: Regional Temperatures and Precipitation. *Science* **1995**, *269*, 676–679. [CrossRef] [PubMed]
40. NOAA NCEI. Extended Reconstructed SST (ERSST) Indices. Available online: https://www.ncei.noaa.gov/pub/data/cmb/ersst/v5/index/ (accessed on 15 January 2026).
41. World Bank. World Development Indicators. Available online: https://databank.worldbank.org/source/world-development-indicators (accessed on 15 January 2026).
42. Gommers, R.; Virtanen, P.; Haberland, M.; Burovski, E.; Reddy, T.; Weckesser, W.; Nelson, A.; Oliphant, T.E.; Cournapeau, D.; Polat, I.; et al. *scipy/scipy: SciPy 1.18.1*; Version v1.18.1; Zenodo: Geneva, Switzerland, 2026. [CrossRef]
43. Harris, C.R.; Millman, K.J.; van der Walt, S.J.; Gommers, R.; Virtanen, P.; Cournapeau, D.; Wieser, E.; Taylor, J.; Berg, S.; Smith, N.J.; et al. Array Programming with NumPy. *Nature* **2020**, *585*, 357–362. [CrossRef] [PubMed]
44. Dickey, D.A.; Fuller, W.A. Distribution of the Estimators for Autoregressive Time Series with a Unit Root. *J. Am. Stat. Assoc.* **1979**, *74*, 427–431. [CrossRef]
45. Phillips, P.C.B.; Perron, P. Testing for a Unit Root in Time Series Regression. *Biometrika* **1988**, *75*, 335–346. [CrossRef]
46. Granger, C.W.J.; Newbold, P. Spurious Regressions in Econometrics. *J. Econom.* **1974**, *2*, 111–120. [CrossRef]
47. Schreiber, T.; Schmitz, A. Surrogate Time Series. *Phys. D Nonlinear Phenom.* **2000**, *142*, 346–382. [CrossRef]
48. Luo, J.J.; Masson, S.; Behera, S.; Yamagata, T. Seasonal Climate Predictability in a Coupled OAGCM Using a Different Approach for Ensemble Forecasts. *J. Clim.* **2005**, *18*, 4474–4497. [CrossRef]

49. Wolter, K.; Timlin, M.S. El Niño/Southern Oscillation Behaviour Since 1871 as Diagnosed in an Extended Multivariate ENSO Index (MEI.ext). *Int. J. Climatol.* **2011**, *31*, 1074–1087. [CrossRef]
50. Liashenko, O.; Pavlov, K.; Pavlova, O. *Replication Data and Code for: Global Food Security in a Climate-Oscillating World: Spectral Evidence and Early Warning Implications for Sustainable Food Systems [Data Set]*; Zenodo: Geneva, Switzerland, 2026. [CrossRef]

Disclaimer/Publisher's Note: The statements, opinions and data contained in all publications are solely those of the individual author(s) and contributor(s) and not of MDPI and/or the editor(s). MDPI and/or the editor(s) disclaim responsibility for any injury to people or property resulting from any ideas, methods, instructions or products referred to in the content.